

Higher-order triangular spectral element method with optimized cubature points for seismic wavefield modeling



Youshan Liu ^{a,*}, Jiwen Teng ^a, Tao Xu ^{a,b}, José Badal ^c

^a State Key Laboratory of Lithospheric Evolution, Institute of Geology and Geophysics, Chinese Academy of Sciences, Beijing, 100029, China

^b CAS Center for Excellence in Tibetan Plateau Earth Sciences, Beijing, 100101, China

^c Physics of the Earth, Sciences B, University of Zaragoza, Pedro Cerbuna 12, 50009 Zaragoza, Spain

ARTICLE INFO

Article history:

Received 22 July 2016

Received in revised form 22 January 2017

Accepted 31 January 2017

Available online 7 February 2017

Keywords:

Triangular spectral element method

Dispersion relation

Optimized cubature points

Positive integration weights

Courant–Friedrichs–Lewy numbers

ABSTRACT

The mass-lumped method avoids the cost of inverting the mass matrix and simultaneously maintains spatial accuracy by adopting additional interior integration points, known as *cubature* points. To date, such points are only known analytically in tensor domains, such as quadrilateral or hexahedral elements. Thus, the diagonal-mass-matrix spectral element method (SEM) in non-tensor domains always relies on numerically computed interpolation points or quadrature points. However, only the *cubature* points for degrees 1 to 6 are known, which is the reason that we have developed a *p*-norm-based optimization algorithm to obtain higher-order cubature points. In this way, we obtain and tabulate new cubature points with all positive integration weights for degrees 7 to 9. The dispersion analysis illustrates that the dispersion relation determined from the new optimized cubature points is comparable to that of the mass and stiffness matrices obtained by exact integration. Simultaneously, the Lebesgue constant for the new optimized cubature points indicates its surprisingly good interpolation properties. As a result, such points provide both good interpolation properties and integration accuracy. The Courant–Friedrichs–Lewy (CFL) numbers are tabulated for the conventional Fekete-based triangular spectral element (TSEM), the TSEM with exact integration, and the optimized cubature-based TSEM (OTSEM). A complementary study demonstrates the spectral convergence of the OTSEM. A numerical example conducted on a half-space model demonstrates that the OTSEM improves the accuracy by approximately one order of magnitude compared to the conventional Fekete-based TSEM. In particular, the accuracy of the 7th-order OTSEM is even higher than that of the 14th-order Fekete-based TSEM. Furthermore, the OTSEM produces a result that can compete in accuracy with the quadrilateral SEM (QSEM). The high accuracy of the OTSEM is also tested with a non-flat topography model. In terms of computational efficiency, the OTSEM is more efficient than the Fekete-based TSEM, although it is slightly costlier than the QSEM when a comparable numerical accuracy is required.

© 2017 Elsevier Inc. All rights reserved.

1. Introduction

The spectral element method (SEM) is a spectrally accurate algorithm for solving partial differential equations (PDEs), which combines the geometrical flexibility of the finite element method (FEM) with the accuracy associated with the spec-

* Corresponding author.

E-mail addresses: ysliu@mail.iggcas.ac.cn (Y. Liu), jwteng@mail.iggcas.ac.cn (J. Teng), xutao@mail.iggcas.ac.cn (T. Xu), badal@unizar.es (J. Badal).

tral method [1]. The computational domain can be divided into quadrilateral (hexahedral) [2–4] or triangular (tetrahedral) elements [5–8]. All variables in each element are approximated by high-order polynomials. The solution of discrete PDEs is obtained by using their integral forms. The diagonal mass matrix can be obtained with appropriate discretization elements as well as clever choice of test functions and collocation points (i.e., collocated interpolation and integration points), which leads to a computationally efficient method [2].

The quadrilateral spectral element method (QSEM) relies on a nodal basis derived from Gauss–Lobatto–Legendre (GLL) points (or the tensor products of GLL points) [2]. The GLL points have both near-optimal polynomial interpolation and integration (cubature) properties [9], which allow one to integrate the stiffness matrix of degree $2N - 2$ exactly and to estimate the mass matrix of degree $2N$ using a high-precision quadrature rule with algebraic accuracy of $2N - 1$ [9,10]. Simultaneously, the small Lebesgue constant of the GLL points means that they can generate a well-conditioned nodal basis. Although a quadrilateral grid has been successfully used, it cannot faithfully and flexibly represent extremely complex geometry. Compared to the quadrilateral and hexahedral elements, the triangular and tetrahedral elements are considerably more flexible for practical applications. Despite it is possible to divide each triangle (or tetrahedron) into four quadrilaterals (or hexahedra) at the expense of increasing the number of nodes per element, the quality of the resulting meshes tends to be poor [11]. Therefore, it seems advisable to develop a method that can be directly applied to the simplex.

Bearing highly complex geometries in mind, the SEM on triangular (tetrahedral in 3D) elements is generally preferred [5–8,12–17]. Unfortunately, points analogous to the GLL points in the case of triangle have not been found after 120 years of research on orthogonal polynomials [18]. At present, the points with an optimal polynomial interpolation and integration properties are only known analytically for an interval and their tensor products. Hence, SEM is usually confined to quadrilateral and hexahedral elements. For non-tensor product domains, such as triangular or tetrahedral elements, there is very little analytical knowledge about the location of the optimal points. This problem is still an open issue. As the GLL points in a one-dimensional (1D) case cannot be extended to a two-dimensional (2D) case, the diagonal mass matrix methods on the triangle always resort to numerically computed interpolation points [13,19–21], or quadrature points [14]. Until now, the typical methods used to find these points either optimize the interpolation nodes or the polynomial integration rather than both. In this sense, several attempts have been made to determine these points by minimizing the Lebesgue constant directly or indirectly. Chen and Babuška [20] directly minimized the Lebesgue constant. Bos [19] and Taylor et al. [13] chose node positions that maximize the determinant of the classical Vandermonde matrix, and the resulting nodes are known as *Fekete* points. An alternative and physically motivated approach comes from the observation of Stieltjes [22,23], which indicates that the roots of the Jacobi polynomials coincide with the equilibrium configuration of charges constrained to lie on the bi-unit interval. Hesthaven [21] extended this analogy to compute nodal distributions by seeking equilibrium positions of charges distributed on the triangle with line charges on the boundaries. Some explicit approaches have also been proposed using an easy-to-implement scheme. Warburton [24] made an explicit construction for interpolation nodes on a simplex whose Lebesgue constants are better than or comparable to those of the existing node sets, at least up to the tenth-order interpolation. Blyth et al. [25,26] obtained a Lobatto interpolation grid over the triangle by means of a sequence of increasingly refined grids, whose Lebesgue constants compete with those of more complicated nodal distributions. Following Blyth's [25] idea, Luo and Pozrikidis [27] constructed a Lobatto interpolation grid on a tetrahedron. Pasquetti and Rapetti [17] reviewed the choice of interpolation nodes on the triangle.

For the optimal interpolation points on the triangle, such as the Fekete points [12,19], electrostatic points [21] and minimum Lebesgue constant points [20], although they are all well-conditioned interpolation nodes, the algebraic accuracy of the generalized Newton–Cotes integration based on these nodes reaches only degree N (i.e., the order of the Lagrange polynomials on the triangle) [9,28]. This is a poor approximation of the inner products of the stiffness matrix (degree $2N - 2$) and the mass matrix (degree $2N$) for seismic wave modeling or second-order PDEs [9,10]. Therefore, the poor approximation to the stiffness and mass matrices using the integration formula with accuracy of degree N (i.e., the generalized Newton–Cotes integration) is insufficient to achieve an exponential convergence [29] because the optimal interpolation points are only good for polynomial interpolation but not for the integration property.

To date, some attempts have been made to find a quadrature rule that can integrate a larger space. Cohen et al. [30] made a pioneering work by enriching the polynomial space with additional interior nodes that vanish at the edges and vertices of the elements. They constructed the points that are analogous to the GLL points for degrees 2 and 3 on the triangle, which increases the integration precision and has positive integration weights. Following the similar idea, Mulder [31–33] obtained such points for degrees 4 to 6, and Giraldo and Taylor [9] for degrees 6 to 7. This method is the so-called mass-lumped method, and the integration points are called *cubature* points because they have higher integration accuracy in contrast to the optimal interpolation points. Although Giraldo and Taylor [9] gave the cubature points for degrees 6 to 7, these points are highly unstable for seismic wavefield modeling. For this reason, they adopted a strong low-pass filter (i.e., erfc-log filter) to stabilize the solution at every 20 time steps. In addition, Mulder [33] pointed out that the integration strength given by Giraldo and Taylor [9] is too small. Furthermore, Helenbrook [34] theoretically proved the following property of the integration rule on the triangle: an integration rule with $(N + 1)(N + 2)/2$ integration nodes is not capable of exactly integrating the space spanned by $T(2N - 1) \equiv \{x^m y^n | 0 \leq m, n; m + n \leq 2N - 1\}$, where N is the order of interpolant polynomials; the integration nodes must include three vertices, $N + 1$ points on each edge, and $(N - 2)(N - 1)/2$ points in the interior of the triangle. Following the Helenbrook's work [34], Xu [35] proved that the number of inner-mode nodes must be greater than or equal to $N(N - 1)/2$ if a cubature rule with algebraic accuracy of $2N - 1$ exists on the triangle.

This establishes a theoretical foundation for the cubature points by enriching the polynomial space with additional interior nodes [30].

Generally, the cubature points on the triangle must satisfy the conformity condition: the polynomials of degree N requires $N + 1$ points on each edge of the triangular element (including vertices), which leads to $3N$ points on the element boundaries. At least $(N_f - 2)(N_f - 1)/2$ inner points are required [33] to obtain positive integration weights. Usually N_f (the order of polynomials in the interior of the triangle) larger than N (the order of polynomials on the edges) is required. To avoid accuracy loss after the mass lumping, a quadrature rule that can precisely integrate polynomials up to a degree $N + N_f - 2$ is required, and the polynomials in the interior of the triangle should vanish on the element boundaries. The -2 term is due to the second-order spatial derivatives in the wave equation or second-order PDEs [33,36]. Although the cubature points for degrees 2 to 6 have been obtained by Cohen et al. [30,37] and Mulder [31–33], higher-order cubature points have not been found.

In this paper, we follow the work of Cohen et al. [30], Mulder [31–33] and Chin-Joe-Kong et al. [38] with the target of finding higher-order cubature points. Before addressing this work, we must first ask ourselves whether the superior accuracy of the higher-order FEM (or SEM) allows, or not, a reduction of the number of freedom largely enough to balance its higher cost. This issue has been thoroughly investigated by Jund and Salmon [39]. Although the use of higher-order cubature points increases the number of freedom and the use of higher-order methods decreases the Courant–Friedrichs–Lewy number (CFL, [40–42]), a substantial reduction in computing time can be obtained compared to lower-order schemes. Additionally, higher-order schemes are more efficient in terms of computational storage. Despite the inherent complexity of the FEM and the more restrictive stability limit for the time step, Mulder [31] already showed that the higher-order FEM is superior to the finite difference method (FDM) in terms of the computing time when a given numerical accuracy is required and the velocity model involves some non-trivial structures. Hence, higher-order cubature points are indeed attractive.

Although lower-order cubature points can be obtained analytically with the help of symbolic computing software, such as *Maple*, it does not seem to be powerful enough for higher-order cubature points [39]. Therefore, in this study, we develop an algorithm that can produce definitely positive integration weights with the fewest points. This work is motivated by the pioneering work of Cohen et al. [30] and others related to the FDM by optimizing the dispersion relation [42–47]. In this context, the optimization problem involves a series of nonlinear moment equations. We allow the integration weights and barycentric coordinates to change freely. Even though Heinrichs [48] claimed that the optimal points are not symmetrically arranged, we shall use the symmetry constraint to significantly decrease the number of unknowns and nonlinear equations.

2. Theory

Since the discretization of the wave equation in the application of the higher-order triangular spectral element method (hereafter, TSEM) can be found in many books and papers [15–17,29], here we limit ourselves to present a short review of the theory below.

2.1. Elastic wave equation

In isotropic heterogeneous media, the second-order elastic wave equation is given by

$$\rho \frac{\partial^2 \mathbf{u}}{\partial t^2} = \nabla[(\lambda + \mu)\nabla \cdot \mathbf{u}] + \nabla \cdot (\mu \nabla \mathbf{u}) + \mathbf{f}, \tag{1}$$

with the initial conditions

$$\begin{cases} \frac{\partial}{\partial t} \mathbf{u}(\mathbf{x}, 0) = \mathbf{0} \\ \mathbf{u}(\mathbf{x}, 0) = \mathbf{0} \end{cases}, \tag{2}$$

where $\mathbf{u}(\mathbf{x}, t)$ is the displacement vector in Cartesian coordinates; $\frac{\partial}{\partial t} \mathbf{u}(\mathbf{x}, 0)$ is particle velocity, i.e., the first-order derivative of the displacement vector with respect to time; $\rho(\mathbf{x})$ is the mass density; $\lambda(\mathbf{x})$ and $\mu(\mathbf{x})$ are the Lamé constants; $\mathbf{f}(\mathbf{x}, t) = R(t)\delta(\mathbf{x} - \mathbf{x}_s)$ is the body force or source function located at point \mathbf{x}_s ; $R(t)$ is the source time function; and ∇ is the nabla operator.

Multiplying equation (1) by the time-independent test function vector \mathbf{w} , integrating by parts and applying the Newman boundary condition on boundaries, we obtain the variational form of the wave equation (1) for the i th component of the displacement

$$\int_{\Omega} \rho w_i \frac{\partial^2 u_i}{\partial t^2} d\Omega + \int_{\Omega} (\lambda + \mu) \frac{\partial w_i}{\partial x_i} \frac{\partial u_j}{\partial x_j} d\Omega + \int_{\Omega} \mu \frac{\partial w_i}{\partial x_j} \frac{\partial u_i}{\partial x_j} d\Omega = \int_{\Omega} w_i f_i d\Omega, \tag{3}$$

where the repeated subscripts denote summation over the affected variables; and Ω is the computational domain. In addition, the free surface boundary condition can be satisfied naturally.

To solve numerically the integral equation (3), the computational domain Ω is decomposed into N_e non-overlapping triangular elements Ω_e with the idea of applying to each element using the nonsingular mapping $(x, z) = \mathbf{F}(\xi, \eta)$, which

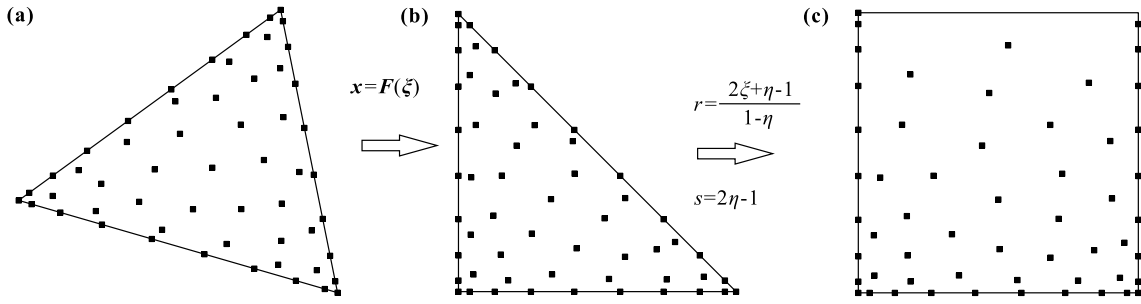


Fig. 1. Schematic diagram that illustrates the coordinate transformation. An affine transformation maps the physical domain (a) to the reference triangular element (b), while Duffy’s transformation maps the reference triangular domain to the standard square (c). The small filled squares represent the 10th-order Fekete points.

defines a transformation from the physical Cartesian coordinate system $\mathbf{x} = (x, z)^T$ to the local reference coordinate system $\xi = (\xi, \eta)^T$ defined in the unit triangle $T = \{(\xi, \eta) | 0 \leq \xi, \eta \leq 1; 0 \leq \xi + \eta \leq 1\}$ (Fig. 1). Hence, the discretization of equation (3) can be done element by element. The details of the discretization process can be found in [15–17,29].

2.2. Shape functions

The shape functions should possess the following property

$$\phi_i(\mathbf{x}_j) = \delta_{ij}, \tag{4}$$

where δ_{ij} is the Kronecker delta symbol. Actually, they are also the Lagrange polynomials on the triangle that can be expanded as

$$\phi_i(\mathbf{x}) = \sum_{j=1}^{M_N} c_i^j \varphi_j(\mathbf{x}), \tag{5}$$

where M_N is the total number of interpolation nodes; c_i^j ($1 \leq j \leq M_N$) are the unknown coefficients corresponding to the i th Lagrange polynomial; and $\{\varphi\}$ is a set of M_N polynomial functions that form a complete base of the N th-order polynomial space, as will be discussed below. Substituting equation (5) into equation (4), the unknown coefficients of the Lagrange polynomials should satisfy the generalized Vandermonde system

$$\mathbf{V} \cdot \mathbf{c}_i = \mathbf{e}_i, \tag{6}$$

where $v_{ij} = \varphi_j(\xi_i)$ are the entries of the generalized Vandermonde matrix \mathbf{V} ; $\mathbf{e}_i = (0, \dots, 0, 1, 0, \dots, 0)^T$ is the i th unit basis vector, i.e., only unit resides in the i th position; and the superscript T represents the transpose operator. The unknown coefficients of the i th Lagrange polynomial are the i th column entries of the inverse generalized Vandermonde matrix \mathbf{V}^{-1} .

Once the solution of the linear system (6) is found, the Lagrange polynomials can be constructed by using equation (5). In contrast to the 1D Lagrange interpolation, both the existence and uniqueness of the solution of (6) are not guaranteed and taken for granted in practical applications. Also, the solution is sensitive to the choice of the orthogonal polynomial basis $\{\varphi\}$. In order to obtain a well-conditioned generalized Vandermonde matrix \mathbf{V} , the Lagrange polynomials are constructed by employing a set of polynomials that enjoy orthogonal or near-orthogonal properties in the triangular spectral element method. Two suitable candidates are available for these polynomials, i.e., the Proriorl–Koornwinder–Dubiner (PKD) [49–51] and Appell [52,53] polynomials. Unfortunately, the condition number of the latter is significantly larger than that of the former [25]. Thus, the former is usually adopted. On the unit or reference triangle, the PKD orthonormal polynomial basis $\{\varphi\}$ is defined as

$$\varphi_k(\xi, \eta) = 2\sqrt{2(2i+1)(i+j+1)} J_i^{0,0} \left(\frac{2\xi + \eta - 1}{1 - \eta} \right) J_j^{2i+1,0} (2\eta - 1)(1 - \eta)^i, \tag{7}$$

where the single index $k = i + j(N + 1) + 1$ depends on two indices varying as $0 \leq i, j \leq N; i + j \leq N, k = 1, \dots, M_N$, being $M_N = (N + 1)(N + 2)/2$; N is the highest order of the Jacobi polynomials; $J_j^{2i+1,0}$ is the j th-order Jacobi polynomial that is a special case of the general Jacobi polynomial $J_j^{\alpha,\beta}$ with indices $\alpha = 2i + 1$ and $\beta = 0$; and $J_i^{0,0}$ is the i th-order Legendre polynomial that is a special case of the general Jacobi polynomial $J_i^{\alpha,\beta}$ with indices $\alpha = \beta = 0$. As the general Jacobi polynomials are orthogonal in the interval $[-1, 1]$ [49–51], we need map spectral elements from the unit triangle to the standard square using the Duffy’s transformation (Fig. 1)

$$\begin{cases} r = \frac{2\xi + \eta - 1}{1 - \eta} \\ s = 2\eta - 1 \end{cases}, \quad -1 \leq r \leq 1, -1 \leq s \leq 1, \tag{8}$$

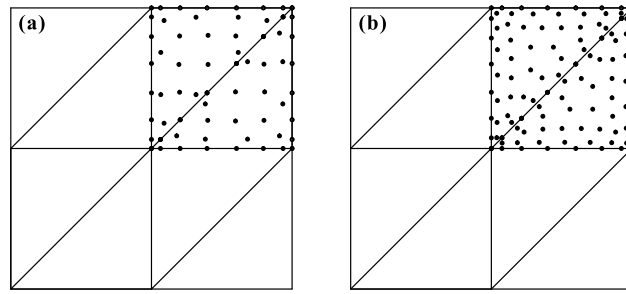


Fig. 2. Periodic grid for the dispersion analysis of the TSEM. The triangles are obtained by dividing one square with sides parallel to the coordinate axes into two isosceles triangles. (a) Fekete points for degree 7; (b) cubature points for degree 7 obtained with the algorithm developed in this study. The unevenly distributed small filled circles represent the distinct classes of the degrees.

where (r, s) is the point on the standard square that is mapped from the point (ξ, η) on the unit triangle. Substituting equation (8) into equation (7), the PKD polynomials that are on the standard square can be written as

$$\varphi_k(r, s) = 2\sqrt{2(2i + 1)(i + j + 1)} J_i^{0,0}(r) \left(\frac{1-s}{2}\right)^i J_j^{2i+1,0}(s). \tag{9}$$

3. Effects of integration on the mass and stiffness matrices

In this study, our essential purpose is to find analogue points to the GLL points in the triangle. Therefore, we have to develop a quadrature rule (or numerical integration rule) that allows us to compute the mass and stiffness matrices without accuracy loss after mass lumping. Because the accuracy of both the mass and stiffness matrices depends on a quadrature rule, to this end, we first carry out a dispersion analysis in an acoustic medium (excluding the effects of Poisson’s ratio or the V_p/V_s ratio) to investigate the effects of numerical integration on the mass and stiffness matrices in the context of spectral element methods. As the dispersion analysis always assumes that the medium is isotropic, homogeneous, unbounded and source free [54–59], we start from the following source free and constant-density acoustic-wave equation

$$\frac{\partial^2 p}{\partial t^2} = c^2 \nabla^2 p, \tag{10}$$

where p is the pressure field; $\partial^2 p/\partial t^2$ is the second-order derivative of the pressure field with respect to time; c is the acoustic velocity; and ∇^2 is the Laplace operator. After discretization, equation (10) becomes

$$M_{ij} \frac{\partial^2 P_j}{\partial t^2} + K_{ij} P_j = 0, \tag{11}$$

where P_j is the pressure wavefield at the j th grid node; $M_{ij} = \int_{\Omega} \phi_i \phi_j d\Omega$ is the mass matrix; and $K_{ij} = c^2 \int_{\Omega} \nabla \phi_i \cdot \nabla \phi_j d\Omega$ is the stiffness matrix. Assuming that the solution is a plane wave, then P_j has the following form

$$P_j(t) = A_j e^{i(\mathbf{k} \cdot \mathbf{x}_j - \omega t)}, \tag{12}$$

where A_j is the wave amplitude at the j th grid node; \mathbf{k} is the wavenumber; \mathbf{x}_j denotes the coordinates at the j th grid node; and ω is the angular frequency. To merely survey the effect of the spatial discretization on numerical dispersion, we only carry out spatial discretization or semi-discretization. Substituting equation (12) into equation (11), we obtain

$$\Lambda M_{ij} P_j = K_{ij} P_j, \tag{13}$$

where $\Lambda = \omega_h^2$ denotes the eigenvalues of the matrix $\mathbf{M}^{-1} \mathbf{K}$ and ω_h is the numerical angular frequency at which the wave travels across the grid. The eigenvalues of equation (13) are real and positive since the matrices \mathbf{M} and \mathbf{K} are symmetric and positive definite, as is well known [60,61]. In general, for higher-order polynomials, we will obtain more eigenvalues than only physical mode. The smallest eigenvalue corresponds to the physical mode [54].

For implementation, we consider isosceles triangles as spectral elements (Fig. 2). Fig. 2(a) shows the Fekete collocation points for degree 7. Throughout this paper, the Fekete points are taken from the work of Briani et al. [62]. Fig. 2(b) shows the cubature points obtained with the algorithm developed in this work. The filled circles represent the distinct classes of freedom. As the eigenvalue problem (13) is tackled on an unbounded domain, we solve it on the periodic grid nodes shown in Fig. 2 (filled circles, [54–56]) to decrease the size of the eigenvalue problem. See the paper of de Basabe et al. [54] for implementation details. In this regular grid, the eigenvalue problem can be formulated as

$$h^2 \Lambda M_{ij} P_j = c^2 K_{ij} P_j, \tag{14}$$

where h denotes the element size; \mathbf{M} is the mass matrix on the unit triangle; and \mathbf{K} is the stiffness matrix with the unit wave velocity. In the following parts, the matrices \mathbf{M} and \mathbf{K} have the same meanings.

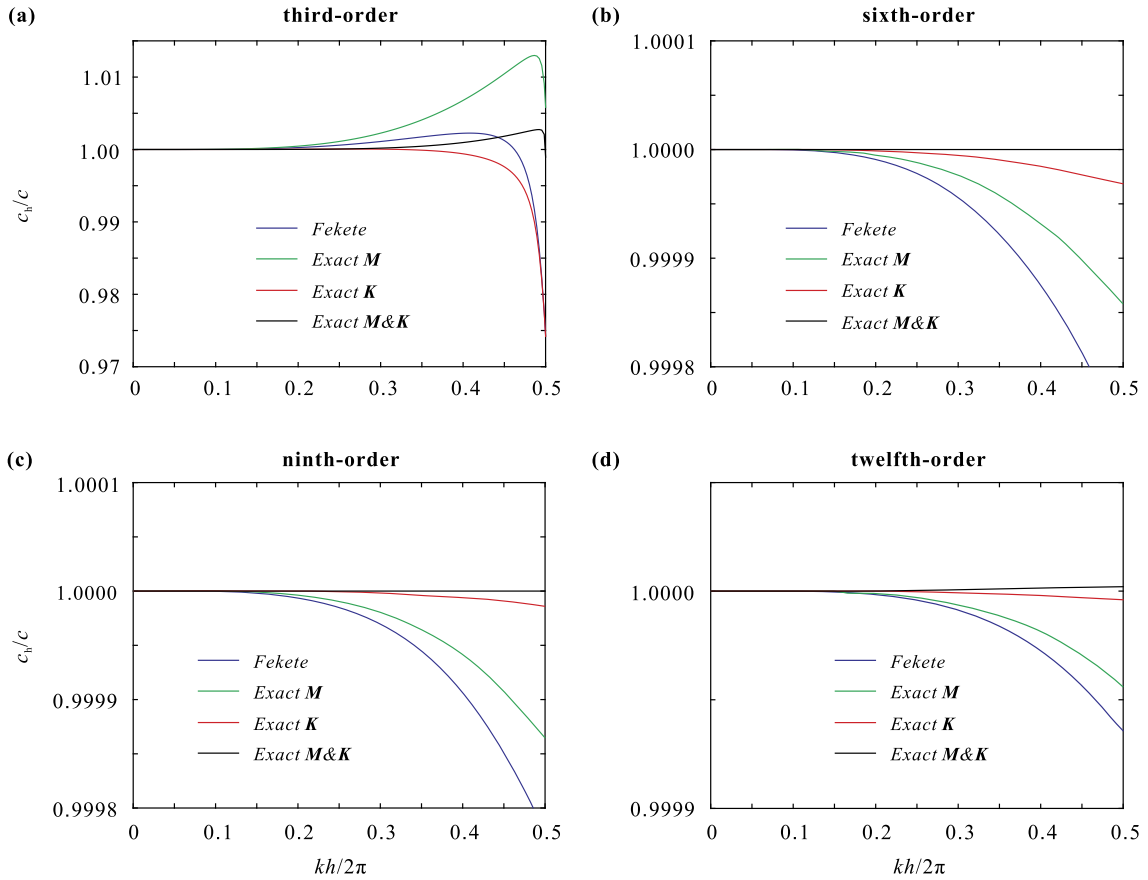


Fig. 3. Dispersion curves using different methods for degrees 3 (a), 6 (b), 9 (c) and 12 (d). The *Fekete* curves (blue lines) are the results of computing both the mass and stiffness matrices by the generalized Newton–Cotes integration used in the Fekete-based TSEM. The curves labeled as *exact M* (green lines) and *exact K* (red lines) mean that only the mass matrix (**M**) or stiffness matrix (**K**) is accurately computed by exact integration, while the other (stiffness or mass) matrix is computed by the generalized Newton–Cotes integration with the Fekete points as interpolation nodes. The notation of *exact M&K* (black lines) indicates that both the mass and stiffness matrices are computed by exact integration with the Fekete points as interpolation nodes. In the horizontal axis, k is the wavenumber and h is the element size. (For interpretation of the references to color in this figure legend, the reader is referred to the web version of this article.)

The dispersion relation is defined as the estimated (numerical) velocity of the wave traveling across the grid normalized by its true value in the medium [63,64]

$$\frac{c_h}{c} = \frac{\sqrt{\Lambda_h}}{2\pi G}, \quad (15)$$

where $c_h = \omega_h/k$ is the *numerical* wave velocity; Λ_h is the smallest eigenvalue of equation (14); and $G = h/L = kh/2\pi$ is the sampling ratio, i.e., the ratio of the element size h to the wavelength L .

Fig. 3 shows the dispersion curves versus the sampling ratio $G \in [0, 0.5]$ using different methods for degrees 3, 6, 9 and 12. As we adopted the regular grid shown in Fig. 2(a) for the dispersion analysis, the dispersion error is maximum along $\theta = 0$, where θ is the angle between the propagation direction of the acoustic wave and x -axis. For this reason, we only show the dispersion relation in the case of $\theta = 0$. In each panel of Fig. 3, the *Fekete* curves (blue lines) are the results corresponding to both the mass and stiffness matrices computed by the generalized Newton–Cotes integration used in the conventional Fekete-based TSEM. The curves labeled as *exact M* (green lines) and *exact K* (red lines) mean that only the mass matrix (**M**) or the stiffness matrix (**K**) is accurately computed by exact integration, while the other matrix (either the stiffness matrix or mass matrix) is calculated by the generalized Newton–Cotes integration with the Fekete points as interpolation nodes. The notation of *exact M&K* (black lines) indicates that both the mass and stiffness matrices are computed by exact integration with the Fekete points as interpolation nodes. In the cases labeled as the *exact M* and the *exact M&K*, their mass matrices are non-diagonal because of the non-collocated interpolation and integration nodes, which implies a depreciation of computational efficiency.

As indicated by Giraldo et al. [9] and Pasquetti et al. [16], both the mass and stiffness matrices estimated by exact integration can yield exponential or spectral convergence, which represents the best dispersion relation among the four tested methods (*Fekete*, *exact M*, *exact K* and *exact M&K*). As can be seen, the Fekete-based TSEM presents the worst

dispersion relation, and the *exact M* shows the second worst, while the *exact K* simultaneously possesses good dispersion properties and a diagonal mass matrix. In general, the *exact K* method is always overwhelmingly more accurate than the *exact M*, which illustrates that an accurate estimation of the stiffness matrix is more significant than an accurate estimation of the mass matrix. In particular, the dispersion curves given by the *exact K* and the *exact M&K* methods for degrees 9 and 12 are highly consistent (Figs. 3c–d). Thus, an optimized cubature formula can accurately compute the stiffness matrix and simultaneously estimate the mass matrix with enough accuracy (although not accurately) is the way to achieve greater accuracy and rapid convergence. This is the idea behind the mass-lumped scheme developed by Cohen et al. [30] and Mulder [31].

4. Cubature points

4.1. Requirements

As pointed out by Fried and Malkus [36], for the second-order PDEs, polynomials up to a degree $q = 2N - 2$ should be integrated exactly by numerical quadrature rule to maintain the convergence. However, this usually leads to zero or negative integration weights [65]. As indicated by Tordjman [65], strictly positive integration weights are needed for stability. Such strictly positive weights can be found if a larger space of polynomials is considered. For triangles, polynomials of maximum degree N_f that have a restriction to the edges of at most a degree $N \leq N_f$ can be used. This integration rule should then be exact for polynomials up to a degree $q = N + N_f - 2$ to avoid accuracy loss [30] and [31]. Therefore, our goal is to find such integration rule or cubature formula. If the integration nodes of the cubature formula (for this reason, they are also called cubature points) include vertices and boundaries, then it is possible to entirely select these nodes as interpolation nodes. Thereby the conformity condition is met. As a result, this cubature formula leads to a fully explicit method as it produces a linear equation system with a diagonal structure that is trivial to invert. This procedure of obtaining a diagonal matrix is called mass lumping. In summary, thus cubature formula must meet the following requirements [33]: i) conformity or continuity of the solution across element boundaries, ii) symmetrical arrangement of nodes, iii) unisolvency, iv) no accuracy loss due to mass lumping, v) positive integration weights, and vi) the fewest number of nodes.

The first condition means that the shape functions have to be continuous across spectral elements, by which the cubature formula has to include three vertices. For the N th-order TSEM, because the restriction on the shape functions defines a unique polynomial of degree N on each edge, and $N + 1$ nodes (including vertices) are required on each edge. Although the second condition, i.e., the symmetry constraint, is not necessary, it can help us reduce the number of moment equations and unknowns substantially [66–68]. The third condition requiring the generalized Vandermonde matrix used to construct the Lagrange polynomials is invertible. The fourth condition requires that the cubature formula (or cubature points) be able to produce spectral convergence or no loss of accuracy. This in return requires that the integration rule must precisely integrate polynomials up to a degree $q = N + N_f - 2$ for the second-order PDEs, where N is the order of the polynomials on the edges and N_f is the order of the polynomials in the interior of the triangle [30–33,36–38,65]. The fifth condition, i.e., positive integration weights, is necessary for the evolution of problems towards stability [69]. Among the cubature formulas that allow a cubature formula to satisfy all these requirements, those involving the fewest number of nodes are the most interesting for the efficiency in practical applications. In this paper, we will refer to the *order* of the TSEM as N instead of N_f .

4.2. Objective function

To develop a cubature formula that meets the above six requirements, first of all we have to construct an objective function to minimize the integration error for polynomials of degrees less than q . In this study, we consider the following p -norm-based objective function

$$E = \left(\sum_{n=1}^{n_e} \left| \sum_{i=1}^{M_N} \omega_i P_n(x_i, y_i) / A_n - 1 \right|^p \right)^{1/p}, \tag{16}$$

where $|\cdot|$ is the absolute value operator; p is a constant; n is the index of the moment equations, $1 \leq n \leq n_e$; i is the index of the integration nodes; M_N is the total number of integration nodes that is identical to the number of interpolation nodes; and $n_e = (q + 1)(q + 2)/2$ is the number of moment equations

$$e_n = \left| \sum_{i=1}^{M_N} \omega_i P_n(x_i, y_i) / A_n - 1 \right|, \tag{17}$$

where A_n is the exact integration of the n th-order monomial $P_n(x, y)$ on the unit triangle; ω_i is the i th integration weight; and (x_i, y_i) is the i th integration node. The meaning of the moment equation is the relative error of the integration formula for the n th-order monomial.

As the optimization problem (16) is highly nonlinear, it is difficult to solve it when q is large. In order to overcome this difficulty, we consider the symmetry constraint on cubature points to decrease the number of the unknowns. As pointed

Table 1

Six equivalent node classes in the triangular element. n_{ci} is the number of nodes in the i th node class. The number of the unknowns in the i th node class is listed in the fourth column. The position of nodes in the i th node class is listed in the fifth column.

Class	Node	n_c	Unknowns	Type
1	(0, 0)	3	1	vertices
2	(1/2, 0)	3×1	1	edge midpoints
3	(α , 0)	3×2	1 + 1	interior edge points
4	(1/3, 1/3)	1	1	center
5	(β , β)	3	1 + 1	interior
6	(δ , γ)	6	2 + 1	interior

out by Keast et al. [66] and Keast [67,68], the symmetric cubature formula just needs to restrict the monomials $P(x, y)$ to those of the form

$$P_{l,m}(x, y) = (xy)^l(1 - x - y)^m, \tag{18}$$

being

$$\begin{cases} 0 \leq 2l + m \leq q \\ 0 \leq m \leq l \end{cases}. \tag{19}$$

This further reduces the number of moment equations under this condition. Therefore, objective function (16) becomes

$$E = \left(\sum_{n=1}^{n_e} \left| \sum_{i=1}^6 \sum_{j=1}^{R_i} v_{i,j}^2 \sum_{k=1}^{n_{ci}} P_{l,m}(x_{i,j,k}, y_{i,j,k}) / A_n - 1 \right|^p \right)^{1/p}, \tag{20}$$

where n_e is the number of moment equations under the condition (19); here, i is the index of the node class; $v_{i,j}^2 = \omega_{i,j}$ is the integration weight to guarantee a positive value; the superscript R_i is the number of the i th node class, and the respective numbers of all these node classes form the so-called integration rule pattern (or integration rule structure), i.e., $\mathbf{R} = (R_1, R_2, \dots, R_6)^T$, (for the detailed definition of the rule pattern please see the next subsection); n_{ci} is the number of nodes in R_i (the corresponding value is listed in Table 1); the total number of the i th (node) class is $n_{ci} \cdot R_i$, being $\mathbf{n}_c = (3, 3, 6, 1, 3, 6)$; and j is the index of the rule pattern. Under the condition (19), the exact integration of the monomial (18) on the unit triangle is

$$A_n = \int_0^1 dx \int_0^{1-x} dy P_{l,m} = \frac{(l!)^2 m!}{(2l + m + 2)!}. \tag{21}$$

Usually, N_f is larger than N , which gives the cubature formula a chance to obtain higher integration accuracy and positive integration weights. On the unit triangle $T = \{(x, y) | 0 \leq x, y \leq 1; 0 \leq x + y \leq 1\}$, the space of the interior polynomials can be expressed by $P_{N_f-3} \times [b]$, being $[b]$ the subspace generated by the bubble function $b = xy(1 - x - y)$ and P_{N_f-3} the PKD polynomial of degree $N_f - 3$. On the three boundaries, the boundary polynomials P_N can be spanned by the product of the functions $x(1 - x - y)$, xy and $y(1 - x - y)$ by the PKD polynomial of degree $N - 2$. Thus, the total space of the Lagrange polynomials consists of $P_N \oplus P_{N_f-3} \times [b]$. After determining the interior and boundary polynomials, the Lagrange polynomials can be constructed by using equation (5). Therefore, the total number of nodes increases from $(N + 1)(N + 2)/2$ in the standard element to $3N + (N_f - 2)(N_f - 1)/2$.

4.3. Rule pattern

Keeping the symmetry constraint in mind, the solution of the nonlinear optimization problem (20) consists of six node classes in the triangular element. Consequently, we should first determine an integration rule pattern. As mentioned in the previous section, the numbers of each node class \mathbf{R} comprise the rule pattern, i.e., $\mathbf{R} = (R_1, R_2, \dots, R_6)^T$. In any case, $R_1 = 1$ since three vertices of the triangle must be included for conformity. Thus, the total number of nodes corresponding to the first class is $3 \times 1 = 3$ (i.e., the three vertices). If and only if N is even $R_2 = 1$ and the total number of nodes corresponding to the second node class $3 \times 1 = 3$ (i.e., the three midpoints on each edge), otherwise $R_2 = 0$. $R_3 = \lfloor \frac{N-1}{2} \rfloor$, where $\lfloor \cdot \rfloor$ represents the integer-valued function. However, the values of R_4, R_5 and R_6 depend on N_f so that they must satisfy the condition $R_4 + 3R_5 + 6R_6 \geq (N_f - 2)(N_f - 1)/2$, which ensures that the order of polynomials in the interior of the triangle is at least N_f .

These node classes, together with the number of nodes in each class, the location of the nodes, and the number of unknowns are listed in Table 1. The first, second and fourth classes have only one unknown, i.e., one integration weight. The third class has two unknowns, i.e., one nodal coordinate α and one integration weight. The fifth class also has two unknowns, i.e., one nodal coordinate β and one integration weight. The sixth class has three unknown, i.e., two nodal

Table 2
All equivalent nodes for the six node classes considered previously (listed in Table 1).

Class	Unknowns	Node coordinates					
1	–	(0, 0)	(0, 1)	(1, 0)	–	–	–
2	–	(1/2, 0)	(0, 1/2)	(1/2, 1/2)	–	–	–
3	α	(α , 0)	(0, α)	(1 – α , 0)	(0, 1 – α)	(α , 1 – α)	(1 – α , α)
4	–	(1/3, 1/3)	–	–	–	–	–
5	β	(β , β)	(1 – 2 β , β)	(β , 1 – 2 β)	–	–	–
6	δ, γ	(δ, γ)	(γ, δ)	($\delta, 1 – \delta – \gamma$)	(1 – $\delta – \gamma, \delta$)	($\gamma, 1 – \delta – \gamma$)	(1 – $\delta – \gamma, \gamma$)

coordinates (δ, γ) and one integration weight. Only one node in each class have to be listed because the others can be easily enumerated since they are symmetrically arranged [33]. The details can be seen in Table 2. Given a rule pattern \mathbf{R} , the total number of integration nodes is

$$M_N = n_{c1}R_1 + n_{c2}R_2 + n_{c3}R_3 + n_{c4}R_4 + n_{c5}R_5 + n_{c6}R_6. \tag{22}$$

Correspondingly, the total number of unknowns is

$$n_u = R_1 + R_2 + 2R_3 + R_4 + 2R_5 + 3R_6. \tag{23}$$

For example, if we take fourth-order cubature points, $N = 4$, and being $\mathbf{R} = (1, 1, 1, 0, 2, 0)$, the total number of integration nodes is 18, while the total number of unknowns is 8. Analogously, if we take fifth-order cubature points, $N = 5$, and being $\mathbf{R} = (1, 0, 2, 0, 3, 1)$, the total number of integration nodes is 30, while the total number of unknowns is 11.

4.4. Nonlinear conjugate gradient method

At present, the cubature points in the triangle are known for degrees 1 to 6 [30–33,36–38,60]. For low-order cases, this system can be solved manually. However, in general, a numerical algorithm seems to be the only option for higher-degree elements. In this study, we will use a nonlinear conjugate gradient (CG) method to solve the nonlinear optimization problem (20) for degrees higher than 7. With this purpose, we adopt the following DY version nonlinear CG method [70]

$$\begin{cases} \beta_k = \max \left\{ 0, \frac{\mathbf{g}_k^T \mathbf{g}_k}{\mathbf{d}_{k-1}^T \mathbf{g}_k} \right\} \\ \mathbf{d}_k = \begin{cases} -\mathbf{g}_k, & k = 1 \\ -\mathbf{g}_k + \beta_k \mathbf{d}_{k-1}, & k > 1 \end{cases} \\ \mathbf{x}_{k+1} = \mathbf{x}_k + \alpha_k \mathbf{d}_k \end{cases} \tag{24}$$

where k is the iteration index; \mathbf{g}_k is the Jacobian vector or gradient at the k th iteration; \mathbf{d}_k is the descent direction; $\mathbf{y}_{k-1} = \mathbf{g}_k - \mathbf{g}_{k-1}$ is the gradient change; \mathbf{x}_k is the solution; and α_k is a step-length obtained by linear search [71]. The way of choosing the parameter β leads to distinct versions of the nonlinear CG methods. Although different versions of CG update parameters β have been developed to date [72,73], the DY version seems to us the fastest and most effective for addressing the optimization problem (20) according to our numerous tests. To obtain the best solution, we compute the analytical gradient of objective function (20) with respect to the unknowns.

For each degree N , we first solve the optimization problem (20) using the DY version nonlinear CG method (24). The stopping criterion is whether the cubature formula can precisely integrate polynomials up to a degree q under the condition of the maximum relative error $\varepsilon \leq 10^{-9}$, being

$$\varepsilon = \max_{1 \leq n \leq ne} \left| \sum_{i=1}^6 \sum_{j=1}^{R_i} v_{i,j}^2 \sum_{k=1}^{n_{ci}} P_{l,m}(x_{i,j,k}, y_{i,j,k}) / A_n - 1 \right|. \tag{25}$$

This condition is called the precision condition.

4.5. Initial solution

Since the local optimization methods depend strongly on the initial solution, the selection of this initial solution is significant for calculation purpose. Therefore, we initially use the symmetric nodes given by Warburton [24] and Blyth et al. [25] as the initial distribution of integration nodes. Once the initial nodal coordinates are set, the initial integration weights are obtained from the following overdetermined equation system

$$\sum_{i=1}^6 \sum_{j=1}^{R_i} v_{i,j}^2 \sum_{k=1}^{n_{ci}} P_{l,m}(x_{i,j,k}, y_{i,j,k}) = A_n. \tag{26}$$

It is noteworthy that the square root of the integration weight is updated instead of the integration weight itself, which ensures a positive integration value and expands the solution space. Although the final solution of (20) with the GLL points on boundaries is appealing because it can couple with the quadrilateral SEM, we cannot obtain such cubature rule that satisfies the precision condition (25).

4.6. Stability condition

To select the best final solution among all those that satisfy the precision condition (25), another criterion is that the solution must have the largest CFL number in addition to the fewest number of nodes. By recovering the source-free and constant-density acoustic-wave equation and after discretization of the temporal derivative in (11) by the second-order leapfrog scheme, we obtain the following eigenvalue problem

$$4 \frac{\sin^2(\omega_h \Delta t/2)}{\Delta t^2} h^2 M_{ij} P_j = c^2 K_{ij} P_j. \tag{27}$$

The CFL number is defined as [54]

$$p = \frac{\Delta t \cdot c_{\max}}{h_{\min}}, \tag{28}$$

where c_{\max} denotes the maximum velocity and h_{\min} denotes the minimum element size. Thus, substituting equation (28) into equation (27), we obtain

$$\frac{p}{2} \sqrt{\Lambda} = \sin^2(\omega_h \Delta t/2) \leq 1, \tag{29}$$

where Λ is the eigenvalue of the matrix $\mathbf{M}^{-1}\mathbf{K}$. The CFL number becomes

$$p \leq CFL = \min\left(\frac{2}{\sqrt{\Lambda}}\right) = \frac{2}{\sqrt{\Lambda_{\max}}}, \tag{30}$$

where Λ_{\max} is the maximum eigenvalue. The larger the CFL number, the larger the time interval Δt is allowed.

4.7. Consistency condition

The nonlinear optimization problem derived from the objective function (20) is difficult to solve, especially for higher-order cases because the system is highly nonlinear with respect to the parameters. In these cases, the solvability of the system can help us determine a rule pattern to find potential solutions. The requirement is that the number of the moment equations (n_e) does not exceed the number of unknowns (n_u), i.e., $n_u \geq n_e$ [33,38]. This results in a set of inequalities that is called the consistency condition [38]. Although this condition is necessary and sufficient for the linear independence of the equations of the system, it is neither necessary nor sufficient for the existence or/and uniqueness of the solution of the nonlinear equation system [38]. Even though the consistent systems that satisfy consistency condition may fail to obtain solutions, while inconsistent systems may still have solutions due to peculiar degenerations of the nonlinear terms. However, this consistency condition provides a good starting point for a systematic search of possible solutions because it significantly narrows the range of admissible solutions.

4.8. Solving process

For a given order N , we first give a rule pattern and start from the standard element (i.e., $N_f = (N - 2)(N - 1)/2$) to solve the optimization problem (20). We then try all possible rule patterns that satisfy the consistency condition $n_u \geq n_e$ and solve the optimization problem (20) using the nonlinear CG method (24). Once the solutions satisfying the precision condition (25) are found, we choose the solution that involves the fewest number of nodes and the largest CFL number [40,41] as the final solution. Otherwise, we increase N_f and try all possible rule patterns until success is achieved. We repeat this process for each given degree N . Although this solving process of nonlinear optimization is rather exhausting, the solution is found once and for all.

4.9. Form of functionals

As for the form of the objective function, we first tried the commonly used maximum norm, L1-norm (the least-absolute-value norm), as well as L2-norm (the least-squares norm). Unfortunately, the solution obtained by these functionals does not satisfy the stopping criterion or the precision condition (25) even after ten million iterations; only the p -norm objective function (20) provides a desirable solution according to the precision condition within ten thousand iterations. Lastly, after several trials and experiments, we found that $p = 3$ is the most efficient option for this parameter. In this study, we obtain new cubature formulas in the triangle for degrees 7 to 9. Although Jund and Salmon [39] also attempted a CG method-based numerical algorithm to obtain a cubature formula, they did not succeed. We attribute our success to the choice of the form of the objective function, the version of the nonlinear CG method and the initial solution.

Table 3

Rule patterns for the polynomials of degrees 7 to 9 on the triangle. N is the degree on the edges; and N_f is the degree in the interior of the triangle. The integration is exact up to a degree q . \mathbf{R} is the number of each node class. The number of equations and unknowns (the square root of integration weights together with the position parameters) are n_e and n_u , respectively. The total number of nodes or degrees of freedom is M_N .

N	N_f	q	\mathbf{R}						n_e	n_u	M_N
			1	2	3	4	5	6			
7	10	15	1	0	3	0	4	4	27	27	57
8	11	17	1	1	3	0	5	5	33	33	69
9	12	19	1	0	4	1	4	7	40	39	82

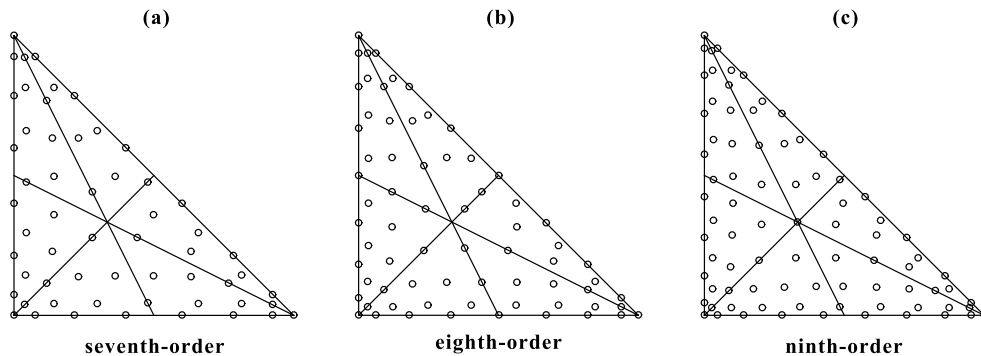


Fig. 4. Distributions of the cubature points for degrees 7 (a), 8 (b), and 9 (c).

5. Optimized cubature formulas

The cubature formulas for degrees 1 to 6 are listed in the paper of Cohen et al. [30,37] and Mulder [32,33]. Now, we obtain three new cubature formulas on the triangle for degrees 7 to 9 using the p -norm-based optimization algorithm in section 4.2. The maximum relative errors according to the precision condition (25) are 3.66×10^{-15} , 5.11×10^{-14} and 4.68×10^{-10} , respectively. These rule patterns are listed in Table 3. The integration weights and nodal position parameters are tabulated in Table 4. For each node class, only one equivalent node and corresponding integration weight are listed. Fig. 4 shows the distribution of the new cubature points for degrees 7 to 9. In general, the integration nodes concentrate toward edges and vertices of triangles. Even though the consistency condition $n_u \geq n_e$ can serve as a guide to find a potential solution, we still obtain a solution for degree 9 that violates the consistency condition (see Table 4).

In Table 5, we tabulate the CFL numbers of the Fekete-based TSEM, the cubature-based TSEM, and the TSEM based on the exact M&K method for degrees 1 to 9, respectively. For the second-order Fekete-based TSEM, the mass matrix is not invertible because of zero integration weights at the vertices of the triangle; the eighth- and ninth-order are unstable because of the negative integration weights. In contrast to the Fekete-based TSEM, the cubature-based TSEM always involves positive integration weights. In terms of the CFL number, the cubature-based TSEM yields slightly smaller CFL number compared to the Fekete-based TSEM because of the adoption of additional interior nodes. Obviously, the exact M&K method possesses the largest CFL number, which represents the best case. In particular, for the first-order Fekete-based TSEM, the CFL number is $\sqrt{2}/2$, which is identical to that given by the first-order FDM [63] because the grid in the former is the same as that in the latter.

6. Analysis of the optimized cubature formulas

In this section, we analyze the characteristics of the optimized cubature formulas with respect to the dispersion relation and the interpolation property.

6.1. Dispersion analysis

In order to check the effectiveness of the optimized cubature formulas, we perform a dispersion analysis using the acoustic-wave equation just as we did in section 3. To analyze the numerical dispersion, we adopt the regular grid shown in Fig. 2(b). The angle between the propagation direction of the acoustic wave and x -axis is θ . In Fig. 5, we show the dispersion curves versus the sampling ratio $G \in [0, 0.5]$ for degrees 5, 7, 8 and 9, respectively. In each panel, the blue lines represent the results obtained by the Fekete-based TSEM; the red lines represent the results obtained by the optimized cubature-based TSEM; and the black lines represent the results obtained by the exact M&K method, i.e., computing both the mass and stiffness matrices by exact integration and taking the Fekete points as interpolation nodes. In general, the numerical dispersion becomes increasingly small as the order of polynomials increases. It is obvious that the exact M&K

Table 4

Integration weights and node position parameters for each node class (fifth and sixth columns, respectively). N is the degree on the edges; and N_f is the degree in the interior of the triangle. The integration is exact up to a degree q . For each node class, only one of the integration weights and position parameters are listed, while other equivalent nodes can be numerated according to Table 2. The Courant–Friedrichs–Lewy (CFL) numbers are listed in the seventh column.

N	N_f	q	Class	Position parameters	Weight	CFL	
7	10	15	1	–		0.285938013608177422908429576864364207722246647e–3	0.0124
			3	0.754072058584607102238450693221238907426595688e–1	0.121706011018912698025407070900882899877615273e–2		
				0.214794118323259342062669929873663932085037231	0.197034042387475788818407274050059641012921929e–2		
				0.399642192575304366908284237069892697036266327	0.240053615532905689766707268972822930663824081e–2		
			5	0.383120054623794434323080793092231033369898796e–1	0.492215573731151316561049924303006264381110668e–2		
				0.116397886866850333587031229853892000392079353	0.851990247875026099344530905455030733719468117e–2		
				0.279307735447201610501366531025269068777561188	0.241856163528129629314289417152394889853894711e–1		
				0.478025598639183535443208938886527903378009796	0.134953161703328574499982650536367145832628012e–1		
			6	0.409329514288468490623706941278214799240231514e–1	0.867539511337682596459064399141425383277237415e–2		
				0.144254257323076784391702176435501314699649811	0.122954988026494904662655471838661469519138336e–1		
				0.434090217167561187583402215750538744032382965e–1	0.297304391665864531368868028948782011866569519		
			8	11	17	1	
2	–	0.174615638855299577791857501551930909045040607e–2					
3	0.626469034050353423825896470589214004576206207e–1	0.821801497801303583966292531926001174724660814e–3					
	0.181221884992308013284656453834031708538532257	0.125450892143815829517239368584569092490710318e–2					
	0.330294406902804149606112105175270698964595795	0.161988566731149376785869886674618101096712053e–2					
5	0.312349045401441142988385735179690527729690075e–1	0.334317342574548970884906751166454341728240252e–2					
	0.910013339870765075589886805573769379407167435e–1	0.635309112044524747220375360257094143889844418e–2					
	0.233132130487337080326781801886681932955980301	0.183579445422039459756557988612257759086787701e–1					
	0.380429163398841807541828075045486912131309509	0.207792521384157422015270810788933886215090752e–1					
	0.440932572285039681148077761463355273008346558	0.124318436873909581030783755295487935654819012e–1					
6	0.310037109163131020805881377100376994349062443e–1	0.561914616699831989676816590417729457840323448e–2					
	0.122080239720277691772842842965474119409918785	0.873727223534249133474194337622975581325590611e–2					
9	12	19	1	–		0.120448081380424015665933645813368002563947812e–3	0.0047
			3	0.458329698846264149691975831046875100582838058e–1	0.529499985956480311889704726269201273680664599e–3		
				0.140404487546879924719789300979755353182554245	0.953463885494742731732675800060405890690162778e–3		
				0.277335077044109423738404984760563820600509644	0.117273478268394492837756182268549309810623527e–2		
				0.424448030981071589007314059927011840045452118	0.130490441453531076827776491455779250827617943e–2		
			4	–	0.181633676628870331659637571419807500205934048e–1		
			5	0.264500206705133023010745318970293737947940826e–1	0.220071155442234283119984361576371156843379140e–2		
				0.881199152586077810722642311702657025307416916e–1	0.502801032369663836174566995396162383258342743e–2		
				0.196370316936668592999737370519142132252454758	0.137111414302799571041102666413280530832707882e–1		
				0.484203915186072919585313911738921888172626495	0.760022890412425083245251400398956320714205503e–2		
			6	0.284681282201876273418861273967195302248001099e–1	0.602083610239412779507883755059083341620862484e–2		
				0.206864138209570891380195689635002054274082184	0.428712442664368025002641360288180294446647167e–2		
	0.288170962299329480593712560221320018172264099e–1	0.960856551044226847579921013675630092620849609e–1					
	0.309204996631560480313538619157043285667896271e–1	0.722146654942792173142995793000409321393817663e–2					
	0.340792271649894007445880106388358399271965027	0.842295866408316468154637846055265981703996658e–2					
	0.937329383496212226178911919305392075330018997e–1	0.105192909983540215657082939060273929499089718e–1					
	0.173951851241586602503375047490408178418874741	0.910160384832466896887215312972330139018595219e–2					
	0.995074826620584718117612510468461550772190094e–1	0.164419515993636487782847410699105239473283291e–1					
	0.285979843485077434017682662670267745852470398						
	0.102583520831418611995999867758655454963445663						
	0.400494088948505688740908681211294606328010559						
	0.205236727216005221396954993906547315418720245						
	0.325886121046975840709336580403032712638378143						

Table 5

CFL numbers of the Fekete-based TSEM, cubature-based TSEM, and TSEM based on the *exact M&K* for degrees 1 to 9. The symbol '*' denotes a non-invertible mass matrix because of zero integration weights, while the symbol '-' represents instability because of negative integration weights.

Degree	1	2	3	4	5	6	7	8	9
<i>Fekete</i>	0.7071	*	0.1256	0.0578	0.0499	0.0174	0.0153	-	-
<i>Cubature</i>	0.7071	0.1765	0.1052	0.0553	0.0242	0.0163	0.0124	0.0078	0.0047
<i>Exact M&K</i>	0.4084	0.2358	0.1084	0.0743	0.0520	0.0397	0.0305	0.0247	0.0200

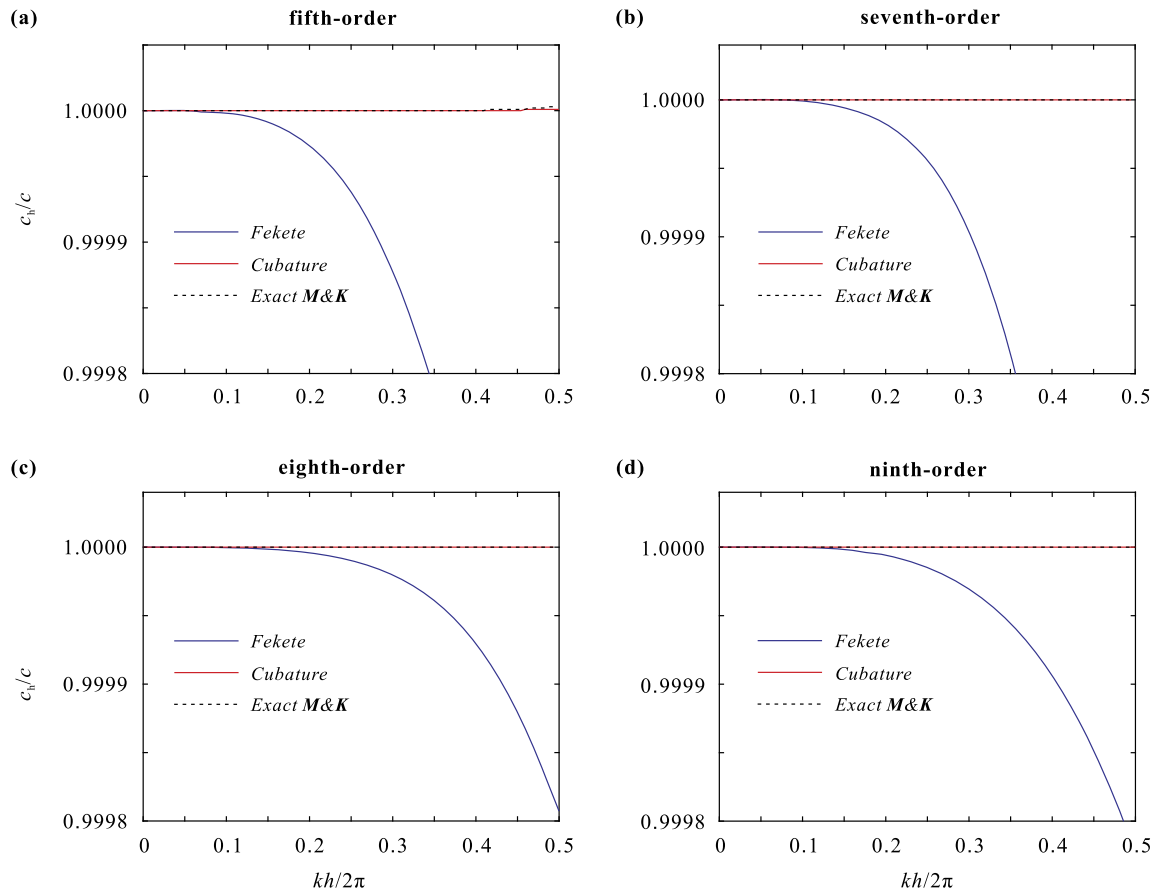


Fig. 5. Dispersion curves using the different methods for degrees 5 (a), 7 (b), 8 (c) and 9 (d). The *Fekete* curves (blue lines) are the results of computing the mass and stiffness matrices by the generalized Newton–Cotes integration used in the Fekete-based TSEM. The curves labeled ‘*cubature*’ (red lines) indicate that both the mass and stiffness matrices are computed by the cubature formulas. The notation of *exact M&K* (black lines) indicates that both the mass and stiffness matrices are computed by exact integration with the Fekete points as interpolation nodes. (For interpretation of the references to color in this figure legend, the reader is referred to the web version of this article.)

method provides the best result for any of the tested degrees (Figs. 5c–d). Compared to the generalized Newton–Cotes integration used in the Fekete-based TSEM, the numerical dispersion obtained by the cubature-based TSEM consistently approaches the best case (*exact M&K*). This demonstrates that the optimized cubature points produce a good numerical dispersion, as expected, which has its counterpart in a substantial improvement of accuracy.

6.2. Interpolation property

So far, we have only paid attention to the accuracy of integration, but what about the interpolation property? In this section, we compute the Lebesgue constant of the optimized cubature points for degrees 1 to 9. As mentioned above, the cubature points for degrees 1 to 6 are given by Cohen et al. [30,37] and Mulder [31–33], while the points for degrees 7 to 9 are obtained by the algorithm developed in this study. The Lebesgue constant on the triangle is defined as [26]

$$L_{M_N} = \max_{\mathbf{x} \in T} L_{M_N}(\mathbf{x}), \quad (31)$$

Table 6
Number of nodes in each spectral element related to the Fekete points and cubature points for degrees 1 to 9.

Degree	1	2	3	4	5	6	7	8	9
<i>Fekete</i>	3	6	10	15	21	28	36	45	55
<i>Cubature</i>	3	7	12	18	30	46	57	69	82

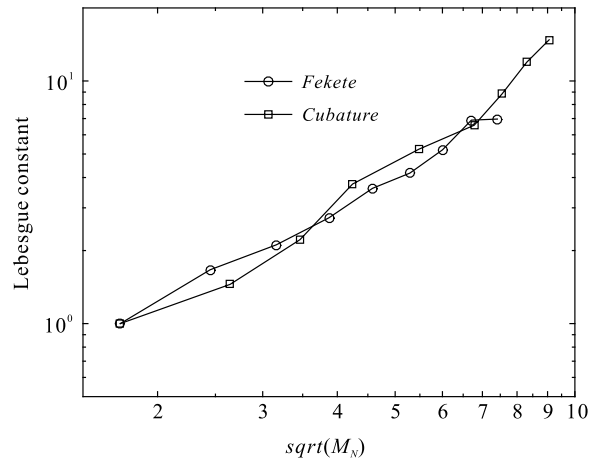


Fig. 6. Lebesgue constants versus the square root of the number of nodes (or degrees of freedom) using the Fekete points and cubature points as interpolation nodes for degrees 1 to 9. The line connecting the circles makes reference to the Fekete points, while the line connecting the squares makes reference to the ‘cubature’ points.

where \mathbf{x} lies on the unit triangle T ; and $L_{M_N}(\mathbf{x})$ is the Lebesgue function

$$L_{M_N}(\mathbf{x}) = \sum_{i=1}^{M_N} |\phi_i(\mathbf{x})|. \tag{32}$$

The Lebesgue constant is a measurement of the interpolation property. The smaller the value, the better the interpolation. If the Lebesgue constant is extremely large, the interpolation function will undergo large oscillations between interpolation nodes, such as in the uniform distribution of nodes. As in this case, the Lebesgue constant increases rapidly with the order of the interpolation polynomials N due to Runge effects, such nodal distribution is suitable only for low-order polynomial expansions, typically for $N \leq 3$ [25]. As a result, the solution of the wave equation via TSEM will depreciate. As indicated by Taylor et al. [12], the numerical evidence suggests that the upper bound of the Lebesgue constant is proportional to $\sqrt{M_N}$. Fig. 6 shows the Lebesgue constants of the Fekete points and cubature points versus the square root of the number of nodes (degrees of freedom) $\sqrt{M_N}$ for degrees 1 to 9. Fortunately, the Lebesgue constant of the cubature points shows an overall consistent trend with respect to that of the Fekete points. This demonstrates that the three new optimized cubature formulas have an interpolation property similar to that given by Cohen et al. [30,37] and Mulder [31–33]. Thus, the optimized cubature formulas provide both high-quality quadrature and well-conditioned interpolants. Generally, the Lebesgue constant of the cubature points is somewhat larger than that of the Fekete points when the number of nodes on the edges is identical, which is due to more nodes existing in the interior of the triangle. The total numbers of the Fekete points and cubature points for degrees 1 to 9 are tabulated in Table 6.

7. Numerical examples

Next, we want to verify two relevant aspects of the TSEM based on the new optimized cubature formulas, i.e., the convergence and efficiency. We adopt it to solve the second-order elastic wave equations (3). The temporal derivative is discretized by the second-order leapfrog scheme.

7.1. Convergence

We consider Lamé’s problem (see Khun [74] for details) to verify the convergence with the new cubature points. In the following, we refer to the conventional Fekete-based triangular SEM as TSEM, and to the optimized cubature-based TSEM as OTSEM. The reference model is a homogeneous half-space with a size of $2 \text{ km} \times 1 \text{ km}$, where the P-wave velocity is 2.0 km/s , the S-wave velocity is 1.15 km/s , and the density is 2.0 g/cm^3 , which corresponds to a Poisson’s ratio value of 0.253 . The top boundary is the free surface, and we apply 0.1 km thick (two spectral elements) perfectly matched layers

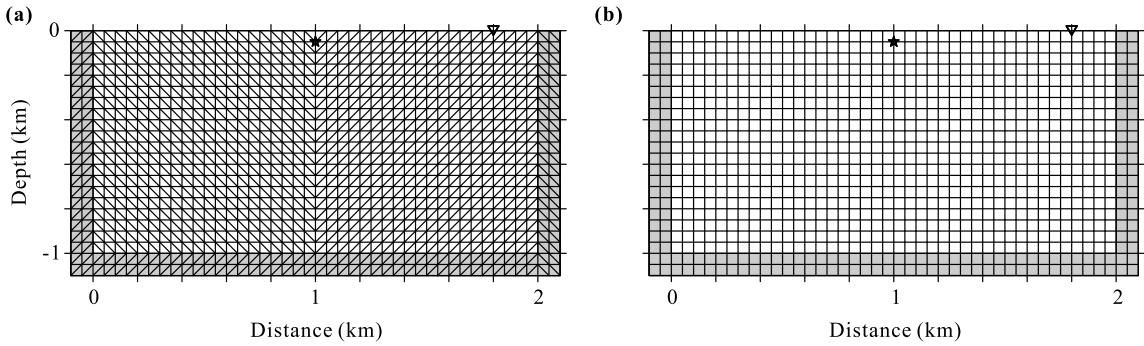


Fig. 7. Meshes conforming a half-space model: (a) by means of triangular elements or (b) square elements, which are used by the TSEM and QSEM, respectively. The pentagrams represent the seismic source located at the point (1.0 km, -0.05 km), while the inverted triangles represent receivers located at the point (1.8 km, 0 km). The shaded domains represent the perfectly matched layers (PMLs).

(PMLs) [75] to suppress spurious reflections from artificial boundaries [10,76]. The model is discretized by isosceles right triangles, being the element size 50 m, which leads to a total number of $2 \times 44 \times 22 = 1936$ spectral elements (including PMLs). Three control points in each triangle are enough to delineate the model. The mesh used for computation with the TSEM and OTSEM is shown in Fig. 7(a), where the shaded bands are PMLs. The pentagram denotes the seismic source, while the inverted triangle denotes a receiver for further analysis. The point source is located at the point (1.0 km, -0.05 km) and consists of a vertical force simulated by a Ricker wavelet with a dominant frequency of $f_0 = 25$ Hz and an onset time of $t_0 = 1/f_0$. Here, we intentionally take a slightly high dominant frequency of the seismic source to avoid the accuracy saturation for high-order schemes. The receiver is deployed exactly on the surface at a horizontal distance of 0.8 km from the source to record the vertical and horizontal displacement components with a record length of 2.5 s. Both the mass and stiffness matrices are precomputed and sparsely stored to improve the computational efficiency [10].

Bearing the CFL number (28) and the values given in Table 5 in mind, the allowable time interval is $\Delta t \leq \frac{CFL \cdot h_{\min}}{c_{\max}}$. Although Jund and Salmon [39] suggested that higher-order discretization in time has to be coupled with higher-order discretization in space to avoid loss of accuracy and convergence. Here, we adopt the second-order leapfrog scheme with an extremely small time step. In this experiment, we take half the maximum allowable time interval as time step, which makes the error generated by temporal discretization negligible.

To check the accuracy of the OTSEM, we first use the following L2-norm and maximum-norm function to investigate the computation error of the numerical solutions calculated at the receiver point (1.8 km, 0 km) (the triangle in Fig. 7a). In the next section, in order to check the accuracy of the OTSEM, we use the L2-norm together with the maximum-norm to obtain the error of the numerical solutions obtained by other family methods at the same receiver point. The L2-norm-based numerical error is estimated as [77]

$$\|e\|_{L2} = \frac{[\sum_{i=0}^{nt} (u_i^h - u_i^a)^2 / (nt + 1)]^{1/2}}{\max_{0 \leq i \leq nt} |u_i^a|}, \quad (33)$$

and the maximum-norm-based numerical error can be defined as

$$\|e\|_{\max} = \frac{\max_{0 \leq i \leq nt} |u_i^h - u_i^a|}{\max_{0 \leq i \leq nt} |u_i^a|}, \quad (34)$$

where nt is the total number of time steps within the considered time window; and u_i^h and u_i^a denote the numerical and analytical solutions [78] at the i th time step located at the receiver, respectively. To eliminate the numerical error due to PMLs, the above numerical errors are counted from time $t = 0$ s up to the time where the earliest spurious reflection just arrives at the receiver. Here, we select seismic records between 0 s and 1 s for the error statistics.

The L2-norm-based computation errors obtained with the OTSEM versus the order of polynomials on the edges ($1 \leq N \leq 9$) are plotted in Fig. 8. The maximum-norm-based computation errors follow a similar trend and are not shown in the illustration. The solid lines joining the squares in each plot show the errors associated with the horizontal (Fig. 8a) and vertical (Fig. 8b) displacement components, respectively. We also compute the slope of each line using the least-squares method to obtain the convergence rate. The dashed lines show the corresponding regression lines for the horizontal and vertical displacement components in semi-logarithmic coordinates. The slopes of these regression lines are $-1/2$ approximately, which is consistent with those (slope of $-1/2$) obtained by Mulder [33]. This supports that the OTSEM yields a comparable convergence compared to that reported by Cohen et al. [30,37] and Mulder [31–33].

7.2. Computational efficiency

In this section, we investigate the computational efficiency of the OTSEM against the conventional Fekete-based TSEM for degrees 7 to 9. Table 6 gives the number of nodes in each spectral element for the Fekete points (TSEM) and optimized

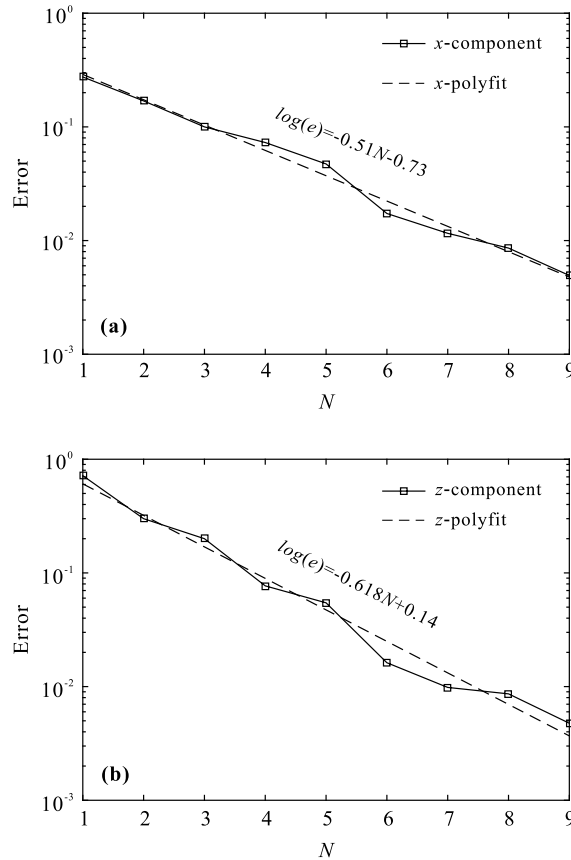


Fig. 8. L2-norm computation errors estimated by the optimized cubature points-based TSEM (OTSEM) versus the order of the polynomials on the edges (N) for degrees 1 to 9. The solid lines joining squares in (a) and (b) show the computation errors associated with the horizontal and vertical displacement components, respectively. The dashed lines show the corresponding regression lines in semi-logarithmic coordinates, respectively.

cubature points (OTSEM). It is obvious that the latter uses more nodes than the former when the order of polynomials on the edges, i.e., N , is identical. However, in terms of accuracy, the TSEM cannot compete with the OTSEM with same N . Indeed, the comparison of the computational efficiency among methods is meaningful only if it is carried out under the condition of a comparable number of nodes in each case. Consequently, the efficiency of the OTSEM against the TSEM is investigated under this condition. Usually, a higher-order TSEM is compared with a lower-order OTSEM. The model remains the same as before, i.e., a homogeneous isotropic half-space. Now we use a Ricker wavelet with a dominant frequency of 15 Hz. The other parameters are identical to those listed in section 7.1. We also compute the numerical solution with the quadrilateral SEM (QSEM) for comparison. The mesh used for computation with the QSEM is shown in Fig. 7(b). As before, the shaded bands represent PMLs. The model is discretized by squares whose size remains 50 m, which leads to a total number of $44 \times 22 = 968$ spectral elements (including PMLs). Taking computational efficiency into consideration, we now adopt the maximum allowable time interval that satisfies the stability condition (CFL number) as time step.

Fig. 9 shows the snapshots of the vertical displacement component at $t = 0.75$ s obtained by the 10th-order TSEM, 14th-order TSEM, 7th-order QSEM and 7th-order OTSEM, respectively. Compared to Figs. 9(c)–(d), Fig. 9(a) reveals an obvious numerical dispersion, while the 14th-order TSEM (Fig. 9b) produces a result comparable to those obtained by the 7th-order QSEM (Fig. 9c) and 7th-order OTSEM (Fig. 9d). This highlights that the accuracy of the conventional TSEM is considerably lower if it is compared with the accuracy of the QSEM and OTSEM. Although in all cases the same PMLs boundary conditions are applied to three boundaries of the model, unlike Fig. 9(d), Figs. 9(a)–(c) exhibit clear spurious artificial reflections coming from the bottom boundary, what stands out even more the good behavior of the OTSEM.

Synthetic seismograms of the vertical displacement component obtained by different methods and degrees N are shown in Fig. 10 (left plot). The seismograms refer to seismic records from a receiver located at the point (1.8 km, 0 km) as seen in Fig. 7. In all cases, the analytical solution [78] is computed to compare with the numerical solutions. We present a zoomed view of all these seismic records within the time window [0.4 s, 1.1 s] for an easier comparison. On the left column, we show the real amplitudes of seismic records obtained by the 7th-, 8th- and 9th-order QSEM and OTSEM, which are compared to those obtained by the 10th-, 12th- and 14th-order TSEM, respectively. For comparison, these methods are divided into three groups with a more or less comparable number of nodes. All seismic records that almost superimpose on the analytical solution reflect the consistency between the numerical solution and analytical solution, while the differences

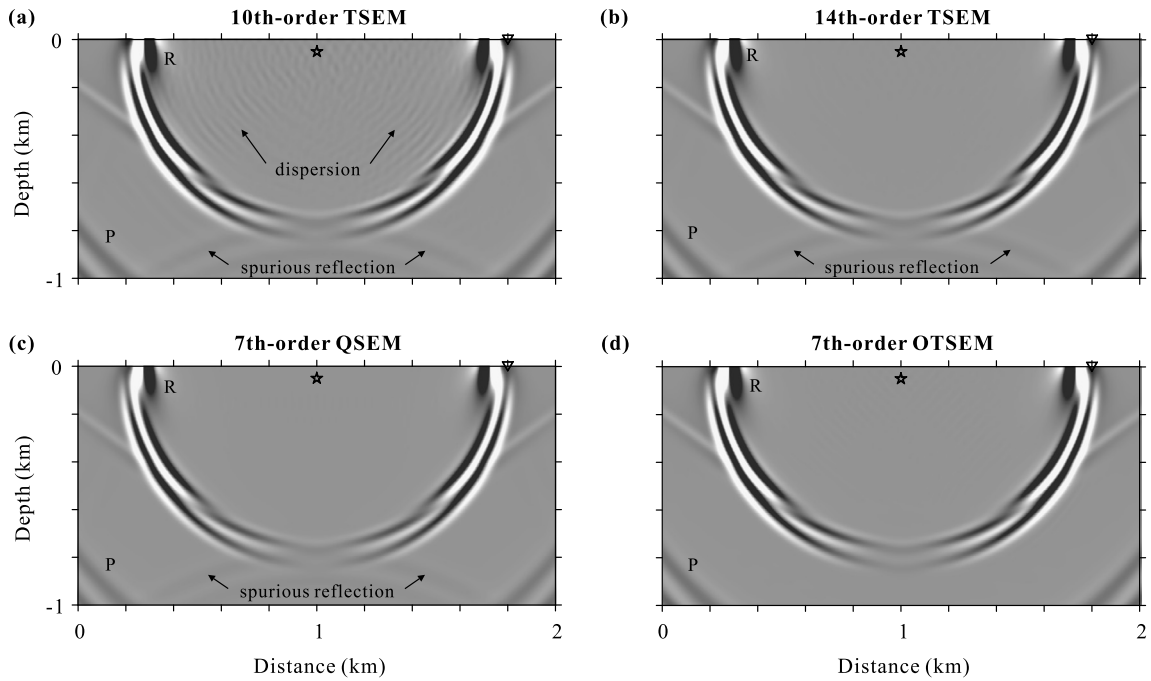


Fig. 9. Snapshots of the vertical displacement component at $t = 0.75$ s. Panels (a), (b), (c) and (d) show the snapshots obtained by the conventional 10th-order TSEM, 14th-order TSEM, 7th-order QSEM and 7th-order OTSEM, respectively. Acronyms: TSEM, Fekete points-based triangular SEM; QSEM, quadrilateral SEM; OTSEM, optimized cubature points-based triangular SEM. The pentagrams represent the seismic source, while the inverted triangles represent the receiver. The letter R indicates the Rayleigh wave and the letter P indicates the P wave.

Table 7

Statistics of computation errors associated with the horizontal and vertical displacement components depending on the used method and degree N (half-space model). The symbols e_{\max} and e_{L2} denote the errors determined by maximum-norm and L2-norm, respectively. M_N denotes the total number of nodes (or degrees of freedom) in each triangular element.

Group	Method	x-component		z-component		M_N
		e_{\max}	e_{L2}	e_{\max}	e_{L2}	
Group1	10th order TSEM	9.552e-2	1.423e-2	1.068e-1	1.740e-2	66
	7th order QSEM	4.330e-3	6.899e-4	7.621e-3	1.104e-3	64
	7th order OTSEM	9.710e-3	1.343e-3	9.538e-3	1.527e-3	57
Group2	12th order TSEM	4.236e-2	6.402e-3	4.764e-2	7.444e-3	91
	8th order QSEM	3.409e-3	4.139e-4	4.841e-3	7.009e-4	81
	8th order OTSEM	2.796e-3	4.856e-4	3.166e-3	5.721e-4	69
Group3	14th order TSEM	4.112e-2	6.469e-3	4.601e-2	7.527e-3	120
	9th order QSEM	2.120e-3	7.350e-4	4.261e-3	6.454e-4	100
	9th order OTSEM	1.389e-3	2.822e-4	2.963e-3	4.484e-4	82

lie in the errors. The computation errors mainly come from the Rayleigh wave due to its shorter wavelength compared to the P-wave. These errors, which are calculated by subtracting the analytical solution from the numerical solution, are also shown within the same time window in Fig. 10 (right plots). From these curves, it is clear that the errors from both the QSEM and OTSEM decrease rapidly with the increasing order of polynomials N , while the error from the TSEM decreases very slowly. Obviously, the accuracy of the OTSEM and QSEM is comparable, but the accuracy of the TSEM is significantly low (about a factor 10). This supports that the optimized cubature points can greatly improve the accuracy of the TSEM.

Table 7 lists the computation errors associated with the horizontal and vertical displacement components depending on the used method and degree N . The symbols e_{\max} and e_{L2} denote the maximum-norm and L2-norm errors, respectively. The errors are estimated within the time window $[0 \text{ s}, 1 \text{ s}]$ to exclude the contribution of spurious reflections coming from artificial boundaries. Again, the accuracy of both the QSEM and OTSEM is comparable and is clearly superior to that of the conventional TSEM. For instance, the accuracy of the 14th-order TSEM (group3) is comparable to that of the 7th-order OTSEM (group1). In general, the accuracy of both the QSEM and OTSEM improves as the polynomial order increases, which is not as evident with the TSEM. In each group, although the OTSEM always uses fewer nodes than the QSEM (see the last column in Table 7), the former produces surprisingly good results compared to the latter. In particular, the accuracy

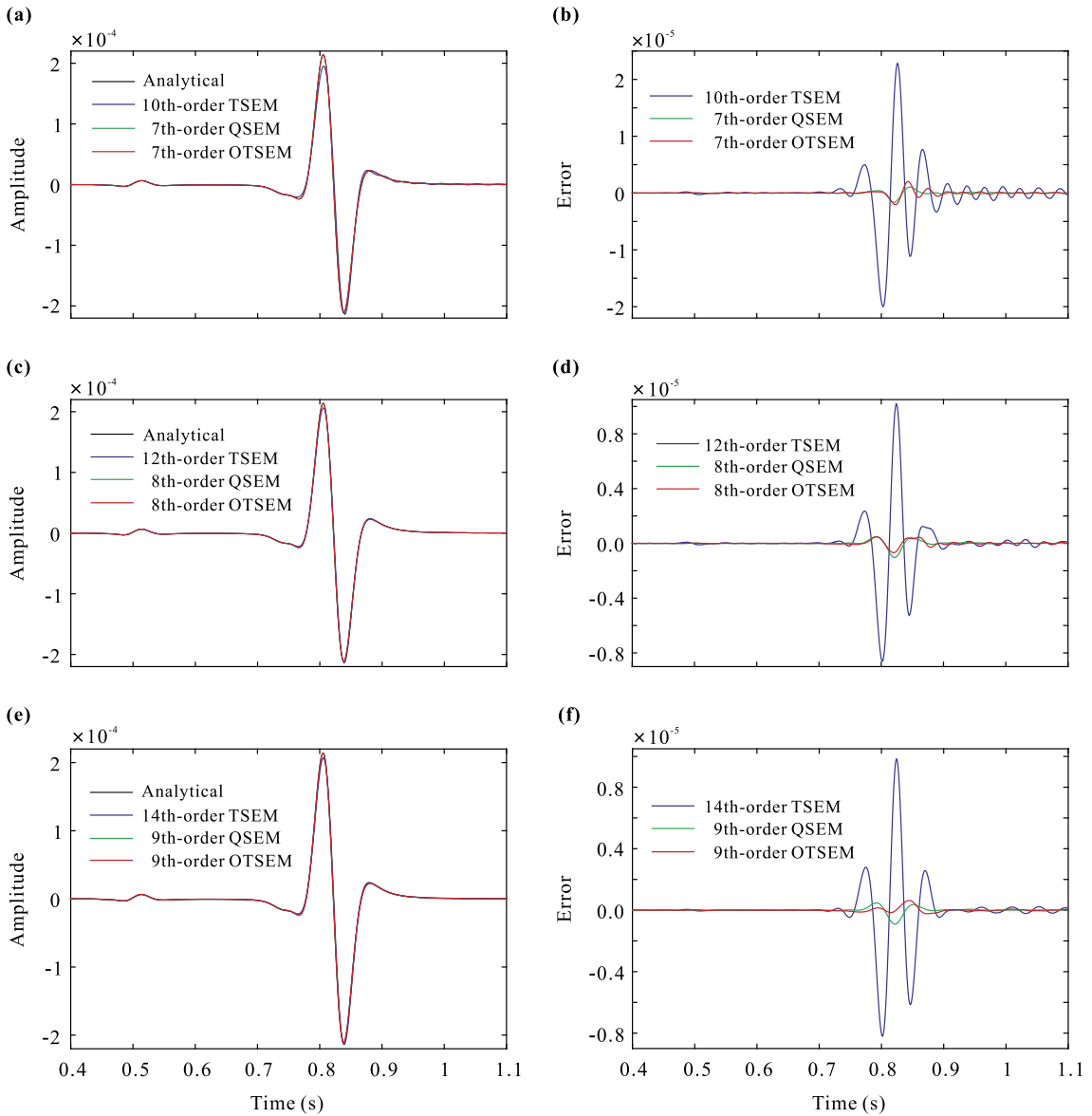


Fig. 10. Windowed synthetic seismograms of the vertical displacement component (left plots) and associated computation errors (right plots) obtained by different methods and degrees N . From top to bottom, the seismic records are divided into three groups for comparison. The blue lines are the results obtained by the TSEM, i.e., the Fekete points-based triangular SEM; the green lines are the results obtained by the QSEM, i.e., the quadrilateral SEM; and the red lines are the results obtained by the OTSEM, i.e., the optimized cubature points-based triangular SEM. The analytical solution (black line) is also included in the graphics (a, c, e) as the reference solution. The computation errors are computed by subtracting the reference solution from the numerical solution. (For interpretation of the references to color in this figure legend, the reader is referred to the web version of this article.)

of the 9th-order OTSEM is slightly higher than that of the 9th-order QSEM (see the last rows of group3 in Table 7). This demonstrates that the OTSEM can compete with the QSEM advantageously or even be better (see group3 in Table 7).

In this half-space model (and in a non-flat topography model presented in the next section), we use the same computational language (Fortran 90, serial code) to implement and execute calculation routines with the Windows operating system on the same computer (Intel(R) Core(TM) i7-4790, 3.60 Hz), which allows us to measure the efficiency of each method. Depending on the polynomial degree N , the efficiency of each method (TSEM, QSEM and OTSEM) is evaluated by the elapsed time, as is shown in Fig. 11. For comparison, the results are displayed as histogram bars for each of the three groups. The respective elapsed times increase passing from the method group1 to group3 (Fig. 11), but the accuracy improves. In each group, although the number of nodes used by the OTSEM is always the smallest (see right column in Table 7), its elapsed time is substantially lower than that of the TSEM but is slightly higher than that of the QSEM (Fig. 11). This is because, on the one hand, the number of elements of the OTSEM is two times larger than the number of elements of the QSEM; on the other hand, the CFL number of the former is smaller than that of the latter. In addition, the stiffness matrix of the OTSEM is

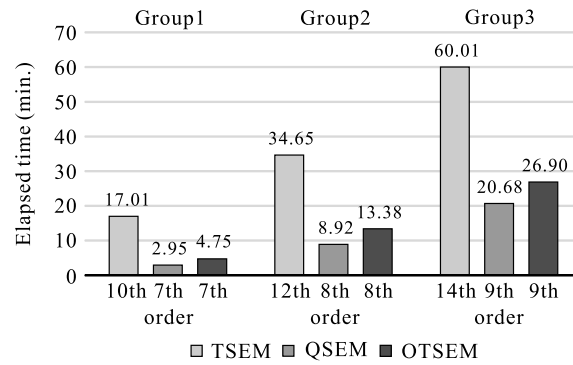


Fig. 11. Histograms of elapsed times corresponding to the numerical examples developed from different methods (TSEM, QSEM and OTSEM) and degrees N (Fig. 10) in the half-space model. Acronyms: TSEM, Fekete points-based triangular SEM; QSEM, the quadrilateral SEM; OTSEM, the optimized cubature points-based triangular SEM. The numbers over the columns indicate the consumption of the elapsed time.

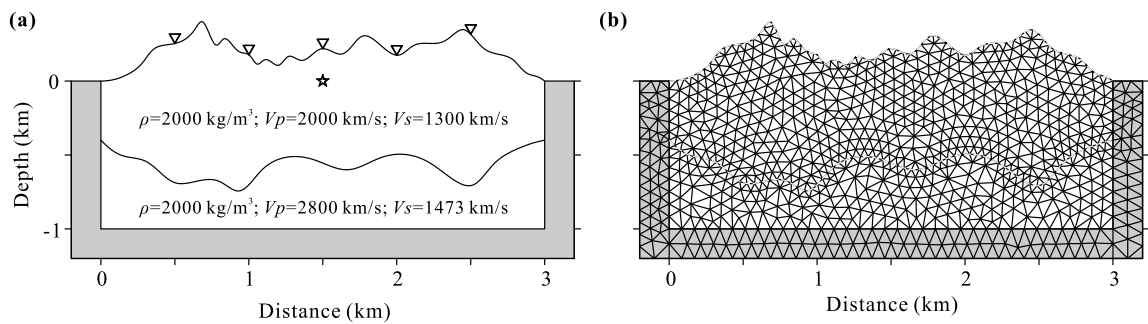


Fig. 12. Two-layer model with irregular topography defined by P- and S-wave velocities and densities (a) and mesh conformed by triangular elements (b). The pentagram represents the seismic source, while the inverted triangles on surface indicate the receivers. The shaded lateral and bottom bands represent the perfectly matched layers (PMLs). The thin white dashed lines included in (b) represent the surface and interface drawn in (a).

much denser than that of the QSEM, which affects the float-point operations involved in the product of the stiffness matrix and the displacement vector. Even so, compared to the conventional TSEM, the computational efficiency of the OTSEM is clearly improved.

7.3. Non-flat topography model

The considered half-space model up to here is fairly simple, so that the straight-edge triangles are sufficient to completely delineate it. However, we now use a non-flat topography model just as one shown in Fig. 12(a) to further test the accuracy of the OTSEM on curvilinear triangular elements. Owing to the existence of rugged topography and an undulated interface, we use six control points in each curved-edge triangular element to accurately delineate the model, especially for those zones close to the surfaces and interface. The discretized model with irregular topography and an undulated interface can be seen in Fig. 12(b). As before, the shaded bands are PMLs. One can appreciate that both the discretized topography and interface (thin white dashed lines) are almost the same as those in the real model, which proves the flexibility of the triangle, even with a coarse grid.

The model size is $3 \text{ km} \times 1 \text{ km}$ and consists of two isotropic layers with variable thickness. The largest undulation extends over 0.4 km . For the upper layer, the density is 2.0 g/cm^3 , V_p is 2.0 km/s and V_s is 1.3 km/s ; for the lower layer, the density is 2.2 g/cm^3 , V_p is 2.8 km/s and V_s is 1.473 km/s . The model is discretized by 1671 triangular elements (including PMLs; see Fig. 12b). The longest edge of the triangles is 0.145 km , while the shortest edge is 0.041 km . To suppress spurious reflections from artificial boundaries, we intentionally adopt relatively thick PMLs (0.2 km). The pentagram represents the seismic source, while the inverted triangles on the surface represent the receivers. The point source is located at the point $(1.5 \text{ km}, 0 \text{ km})$ and consists of a vertical force simulated by a Ricker wavelet with a dominant frequency of 13.2 Hz . The receivers are deployed exactly on the surface at horizontal distances of 0.5 km , 1.0 km , 1.5 km , 2.0 km and 2.5 km to record the horizontal and vertical displacement components with a record length of 5 s . To eliminate the differences from meshes (i.e., differences between the quadrilaterals and triangles), we do not consider the 7th-order QSEM at this point and use only the 10th-order TSEM and 7th-order OTSEM for comparison. Given that the analytical solution for this model is not available, we use the numerical solution obtained by the 9th-order OTSEM as a reference solution. Considering the stability condition, the maximum allowable time intervals are 0.186 ms , 0.181 ms and 0.069 ms when applying the 10th-order TSEM, 7th-order

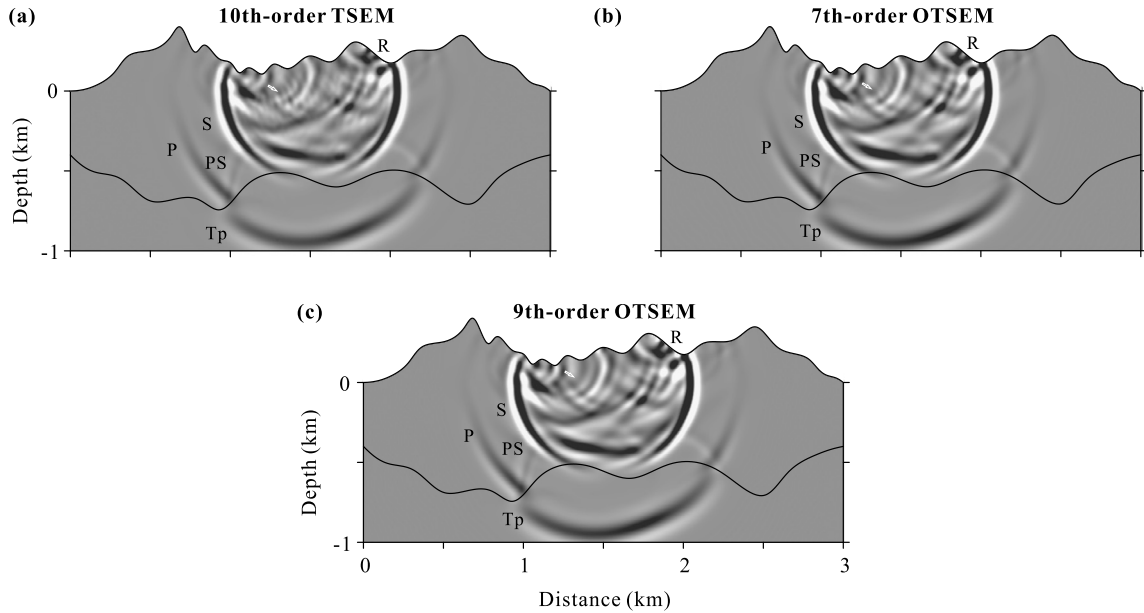


Fig. 13. Snapshots of the vertical displacement component at $t = 0.5$ s. Panels (a), (b), and (c) show the snapshots obtained by the 10th-order TSEM, 7th-order OTSEM, and 9th-order OTSEM, respectively. The small white arrows indicate the serious numerical dispersion (mainly in panel a). Acronyms: TSEM, Fekete points-based triangular SEM; OTSEM, optimized cubature points-based triangular SEM. Notations: P, direct P-wave; S, direct S-wave; Tp, transmitted P-wave; PS, P-to-S converted wave; R, Rayleigh wave.

OTSEM and 9th-order OTSEM, respectively. Nevertheless, we intentionally use much smaller time intervals to eliminate the effects of discretization in time, namely, 0.050 ms, 0.050 ms and 0.025 ms, respectively.

Fig. 13 shows snapshots of the vertical displacement component at $t = 0.5$ s obtained by the 10th-order TSEM, 7th-order OTSEM and 9th-order OTSEM. The real surface and interface (black solid lines) are superimposed on the snapshots. Intuitively, these snapshots are very complex due to the multiple reflected waves from the rugged topography and interface. Even so, the direct P-wave (P), direct S-wave (S), transmitted P-wave (Tp), P-to-S converted wave (PS) and Rayleigh wave (R) can be easily identified. It is obvious that the snapshot obtained by the 10th-order TSEM exhibits serious numerical dispersion in the area surrounded by the wavefront of the direct S-wave (small white arrows in Fig. 13a); this effect does not occur in the two other snapshots computed by the 7th-order (Fig. 13b) and 9th-order OTSEM (Fig. 13c). This demonstrates the relatively low accuracy of the conventional TSEM compared to the OTSEM.

Fig. 14 shows the synthetic traces of the horizontal and vertical displacement components (left plots) obtained by different methods and degrees N at the five receivers deployed on the surface (Fig. 12a). The blue traces are the results obtained by the 10th-order TSEM, while the red traces are the results obtained by the 7th-order OTSEM, respectively. The numerical solution obtained by the 9th-order OTSEM is the reference solution (black traces in Figs. 14a and 14c). The traces computed by the OTSEM better fit the reference solution compared to those calculated by the TSEM. The computation errors are computed by subtracting the reference solution from the numerical solution and are shown with an amplification factor of 5 (Figs. 14b and 14d). As expected, the errors of the TSEM are obviously higher than those of the OTSEM since the numerical dispersion (Fig. 13a) is mainly responsible for the errors. This illustrates that the accuracy of the 7th-order OTSEM is higher than that of the 10th-order TSEM.

Table 8 lists the computation errors associated with the horizontal and vertical displacement components recorded at the five receivers deployed on the surface (Fig. 12), depending on the used method and degree N . The symbols e_{\max} and e_{L2} denote the errors determined by the maximum-norm and L2-norm errors, respectively. The comparison of all these errors further confirms that the accuracy of the 7th-order OTSEM is higher than that of the 10th-order TSEM even for curvilinear triangles. With respect to the computational efficiency, the 10th-order TSEM takes 120.2 minutes, while the 7th-order OTSEM takes 47.5 minutes. Thus, the former consumes almost three times more time than the latter, due to the smaller CFL number and the greater number of nodes compared to the 7th-order OTSEM. This confirms that the OTSEM is more efficient than the conventional TSEM even for curvilinear triangles.

8. Conclusions

The present work focuses on the development of a new spectral element approximation based on the use of triangular elements, new quadrature rule and interpolation points, so that the mass matrix is diagonal. The approach is of nodal type and the set of inner nodes is chosen to achieve a high enough quadrature capability.

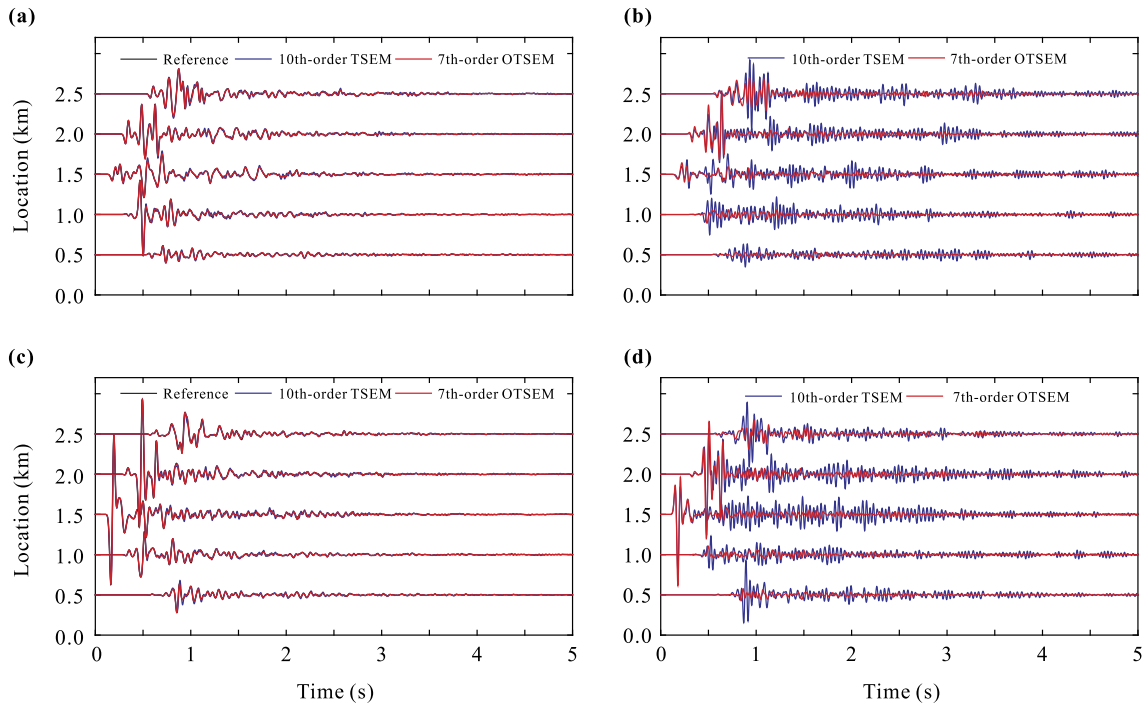


Fig. 14. Synthetic seismograms of the horizontal and vertical displacement components (left plots, a and c) obtained by different methods and degrees N at the five receivers deployed on the surface (Fig. 12). The blue and red traces are the results obtained by the 10th-order TSEM and the 7th-order OTSEM, respectively. The solution obtained by the 9th-order OTSEM is the reference solution (black traces in plots a and c). The real amplitudes are shown in the left column, while the computation errors (numerical solution – reference solution) are shown with an amplification factor of 5 (right plots, b and d). (For interpretation of the references to color in this figure legend, the reader is referred to the web version of this article.)

Table 8

Statistics of computation errors associated with the horizontal and vertical displacement components recorded at the five receivers deployed on surface (Fig. 12a), depending on the used method and degree N . The symbols e_{\max} and e_{L2} denote the errors determined by the maximum-norm and L2-norm, respectively. M_N denotes the total number of nodes (or degrees of freedom) in each triangular element.

Receiver location	Method	x-component		z-component		M_N
		e_{\max}	e_{L2}	e_{\max}	e_{L2}	
0.5 km	10th order TSEM	2.677e-1	4.997e-2	3.883e-1	4.138e-2	66
	7th order OTSEM	8.399e-2	1.609e-2	6.967e-2	1.096e-2	57
1.0 km	10th order TSEM	9.894e-2	1.762e-2	1.627e-1	2.599e-2	66
	7th order OTSEM	4.269e-2	5.659e-3	7.481e-2	1.051e-2	57
1.5 km	10th order TSEM	1.746e-1	3.325e-2	1.458e-1	1.531e-2	66
	7th order OTSEM	9.928e-2	1.402e-2	1.812e-1	1.266e-4	57
2.0 km	10th order TSEM	2.903e-1	3.054e-2	1.628e-1	1.713e-2	66
	7th order OTSEM	2.749e-2	2.478e-2	1.726e-1	1.618e-2	57
2.5 km	10th order TSEM	2.853e-1	3.880e-2	3.052e-1	3.682e-2	66
	7th order OTSEM	1.331e-1	2.110e-2	1.424e-1	1.665e-2	57

First, we analyzed the effects of the numerical integration on the mass and stiffness matrices through the dispersion analysis. This analysis illustrates that an accurate estimation of the stiffness matrix is more significant than the mass matrix. Thus, an optimized cubature formula that can accurately compute the stiffness matrix and simultaneously estimate the mass matrix with enough approximation (although not accurate) is the way to achieve a greater accuracy and rapid convergence. When a larger space of polynomials that vanish on the boundaries is considered, this condition is relaxed by requiring that the quadrature rule can accurately integrate polynomials up to a degree $q = N + N_f - 2$ to avoid accuracy loss after mass lumping.

We have used a p -norm-based objective function along with local optimization method to obtain higher-order cubature points for degrees 7 to 9. The convergence analysis illustrates that the three new cubature formulas allow us to obtain an approximate convergence rate of $O(N^{-1/2})$. We have listed the CFL numbers for the conventional TSEM, the TSEM with both mass and stiffness matrices computed by exact integration, and the optimized cubature point-based TSEM (OTSEM). The developed algorithm always leads to positive integration weights and high integration accuracy so that both the stability over time and spatial accuracy can be maintained simultaneously. In addition, the optimized cubature formulas provide

well-conditioned interpolants. This also avoids the inversion of a wide bandwidth mass matrix because the collocated interpolation and integration points are kept in mind, which leads to a diagonal mass matrix.

We have performed a numerical experiment using a half-space model, which proves that the OTSEM improves the accuracy of the TSEM by approximately one order of magnitude. In particular, the accuracy of the 7th-order OTSEM is even higher than that of the 14th-order TSEM. Compared to the quadrilateral SEM (QSEM), the OTSEM can compete advantageously. In particular, the accuracy of the 9th-order OTSEM is slightly higher than that of the 9th-order QSEM. In terms of convergence, the computation error of the OTSEM decreases exponentially as the polynomial degree increases. In terms of computational efficiency, the OTSEM is more efficient than the TSEM, although it is slightly costlier than the QSEM when a comparable numerical accuracy is considered.

Another numerical experiment conducted on a non-flat topography model and an undulated interface has allowed us to test the accuracy of the OTSEM on curvilinear triangles. In particular, the 7th-order OTSEM is able to generate good results, while the 10th-order TSEM suffers from serious numerical dispersion. In terms of efficiency, the 7th-order OTSEM is significantly more efficient than the 10th-order TSEM.

The new implemented approach is able to achieve a high-order quadrature accuracy, so it is also of interest to solve many other problems besides seismic wavefield modeling, for instance evolution problems with an explicit time marching. However, although the success of the optimized cubature formula is obtained in the triangle, it is not easy to extend to tetrahedral elements in 3D because of the inherent difficulty of the optimization problem.

Acknowledgements

This paper is dedicated to the memory of Prof. Zhongjie Zhang (1964–2013). Fruitful discussions with Professors W.A. Mulder, D. Komatitsch, J. Zhang, S. Liu, and H. Lan are also greatly appreciated. The authors would like to thank the editor Dr. J.S. Hesthaven and two anonymous reviewers for their very attentive reviews and constructive comments. We gratefully acknowledge the financial support for this work contributed by the National Key Research and Development Program of China (grant nos. 2016YFC0600101 and 2016YFC0600201), the National Natural Science Foundation of China (grant nos. 41604076, 41674102, 41674095, 41522401, 41374062 and 41404073), the China Earthquake Administration (grant no. 201408023), and the China Postdoctoral Science Foundation (grant no. 2016M600128).

Appendix A. Supplementary material

Supplementary material related to this article can be found online at <http://dx.doi.org/10.1016/j.jcp.2017.01.069>.

References

- [1] A.T. Patera, A spectral element method for fluid dynamics-laminar flow in a channel expansion, *J. Comput. Phys.* 54 (1984) 468–488.
- [2] Y. Maday, A.T. Patera, Spectral element methods for the incompressible Navier–Stokes equations, in: A.K. Noor, J.T. Oden (Eds.), *State of the Art Surveys on Computational Mechanics*, ASME, New York, 1987, pp. 71–143.
- [3] D. Komatitsch, J.P. Vilotte, The spectral-element method: an efficient tool to simulate the seismic response of 2-D and 3-D geological structures, *Bull. Seismol. Soc. Am.* 88 (1998) 368–392.
- [4] D. Komatitsch, J. Tromp, Introduction to the spectral-element method for 3-D seismic wave propagation, *Geophys. J. Int.* 139 (1999) 806–822.
- [5] S.J. Sherwin, G.E. Karniadakis, A triangular spectral element method: applications to the incompressible Navier–Stokes equations, *Comput. Methods Appl. Mech. Eng.* 123 (1995) 189–229.
- [6] M.A. Taylor, B.A. Wingate, Fekete collocation points for triangular spectral elements, *SIAM J. Numer. Anal.* (1999) 1–23.
- [7] D. Komatitsch, R. Martin, J. Tromp, M.A. Taylor, B.A. Wingate, Wave propagation in 2-D elastic media using a spectral element method with triangles and quadrangles, *J. Comput. Acoust.* 9 (2001) 703–718.
- [8] E.D. Mercerat, J.P. Vilotte, F.J. Sánchez-Sesma, Triangular spectral element simulation of two-dimensional elastic wave propagation using unstructured triangular grids, *Geophys. J. Int.* 166 (2006) 679–698.
- [9] F.X. Giraldo, M.A. Taylor, A diagonal-mass-matrix triangular-spectral element method based on cubature points, *J. Eng. Math.* 56 (2006) 307–322.
- [10] Y.S. Liu, J.W. Teng, H.Q. Lan, X. Si, X.Y. Ma, A comparative study of finite element and spectral element methods in seismic wavefield modeling, *Geophysics* 79 (2014) T91–T104.
- [11] S.J. Owen, A survey of unstructured mesh generation technology, in: *Proceedings of the 7th International Meshing Roundtable*, 1998, pp. 26–28.
- [12] M.A. Taylor, B.A. Wingate, A generalized diagonal mass matrix spectral element method for non-quadrilateral elements, *Appl. Numer. Math.* 33 (2000) 259–265.
- [13] M.A. Taylor, B.A. Wingate, R.E. Vincent, An algorithm for computing Fekete points in the triangle, *SIAM J. Numer. Anal.* 38 (2000) 1707–1720.
- [14] M.A. Taylor, B.A. Wingate, L.P. Bos, A cardinal algorithm for computing multivariate quadrature points, *SIAM J. Numer. Anal.* 45 (2007) 193–205.
- [15] R. Pasquetti, F. Rapetti, Spectral element methods on triangles and quadrilaterals: comparisons and applications, *J. Comput. Phys.* 198 (2004) 349–362.
- [16] R. Pasquetti, F. Rapetti, Spectral element methods on unstructured meshes: comparisons and recent advances, *J. Sci. Comput.* 27 (2006) 377–387.
- [17] R. Pasquetti, F. Rapetti, Spectral element methods on unstructured mesh: which interpolation points?, *Numer. Algorithms* 55 (2010) 349–366.
- [18] D. Braess, Approximation on Simplices and Orthogonal Polynomials, *Int. Ser. Numer. Math.*, vol. 151, 2005, pp. 53–60.
- [19] L. Bos, Bounding the Lebesgue function for Lagrange interpolation in a simplex, *J. Approx. Theory* 38 (1983) 43–59.
- [20] Q. Chen, I. Babuška, Approximate optimal points for polynomial interpolation of real functions in an interval and in a triangle, *Comput. Methods Appl. Mech. Eng.* 128 (1995) 405–417.
- [21] J.S. Hesthaven, From electrostatics to almost optimal nodal sets for polynomial interpolation, *SIAM J. Numer. Anal.* 35 (1998) 655–676.
- [22] T.J. Stieltjes, Sur quelques théorèmes d’algèbre, *C. R. Acad. Sci., Paris* 100 (1885) 439–440 (in French).
- [23] T.J. Stieltjes, Sur les polynômes de Jacobi, *C. R. Acad. Sci., Paris* 100 (1885) 620–622 (in French).
- [24] T. Warburton, An explicit construction of interpolation nodes on the simplex, *J. Eng. Math.* 56 (2006) 247–262.
- [25] M.G. Blyth, C. Pozrikidis, A Lobatto interpolation grid over the triangle, *IMA J. Appl. Math.* 71 (2005) 153–169.

- [26] M.G. Blyth, H. Luo, C. Pozrikidis, A comparison of interpolation grids over the triangle or the tetrahedron, *J. Eng. Math.* 26 (2006) 263–272.
- [27] H. Luo, C. Pozrikidis, A Lobatto interpolation grid in the tetrahedron, *IMA J. Appl. Math.* 71 (2006) 298–313.
- [28] B.A. Wingate, M.A. Taylor, Performance of numerically computed quadrature points, *Appl. Numer. Math.* 58 (2008) 1030–1041.
- [29] F.X. Giraldo, T. Warburton, A nodal triangle-based spectral element method for the shallow water equations on the sphere, *J. Comput. Phys.* 207 (2005) 129–150.
- [30] G. Cohen, P. Joly, N. Tordjman, Higher order triangular finite elements with mass lumping for the wave equation, in: G. Cohen, E. Bécache, P. Joly, J.E. Roberts (Eds.), *Proceedings of the Third International Conference on Mathematical and Numerical Aspects of Wave Propagation*, SIAM, Philadelphia, 1995, pp. 270–279.
- [31] W.A. Mulder, A comparison between higher-order finite elements and finite differences for solving the wave equation, in: J. Désidéri, P. LeTallec, E. Onate, J. Périaux, E. Stein (Eds.), *Proceedings of the Second ECCOMAS Conference on Numerical Methods in Engineering*, John Wiley & Sons, Chichester, 1996, pp. 344–350.
- [32] W.A. Mulder, Higher-order mass-lumped finite elements for the wave equation, *J. Comput. Acoust.* 9 (2001) 671–680.
- [33] W.A. Mulder, New triangular mass-lumped finite elements of degree six for wave propagation, *Prog. Electromagn. Res.* 141 (2013) 671–692.
- [34] B.T. Helenbrook, On the existence of explicit hp-finite element methods using Gauss–Lobatto integration on the triangle, *SIAM J. Numer. Anal.* 47 (2009) 1304–1318.
- [35] Y. Xu, On Gauss–Lobatto integration on the triangle, *SIAM J. Numer. Anal.* 49 (2011) 541–548.
- [36] I. Fried, D.S. Malkus, Finite element mass matrix lumping by numerical integration with no convergence rate loss, *Int. J. Solids Struct.* 11 (1975) 461–466.
- [37] G. Cohen, P. Joly, J.E. Roberts, N. Tordjman, Higher order triangular finite elements with mass lumping for the wave equation, *SIAM J. Numer. Anal.* 38 (2001) 2047–2078.
- [38] M.J.S. Chin-Joe-Kong, W.A. Mulder, V. Veldhuizen, Higher-order triangular and tetrahedral finite elements with mass lumping for solving the wave equation, *J. Eng. Math.* 35 (1999) 405–426.
- [39] S. Jung, S. Salmon, Arbitrary high-order finite element schemes and higher-order mass lumping, *Int. J. Appl. Math. Comput. Sci.* 17 (2007) 375–393.
- [40] R. Courant, K. Friedrichs, H. Lewy, Über die partiellen Differenzgleichungen der mathematischen Physik, *Math. Ann.* 100 (1928) 32–74 (in German).
- [41] P.D. Lax, B. Wendroff, Systems of conservation laws, *Commun. Pure Appl. Math.* 13 (1960) 217–237.
- [42] O. Holberg, Computational aspects of the choice of operator and sampling interval for numerical differentiation in large-scale simulation of wave phenomena, *Geophys. Prospect.* 35 (1987) 629–655.
- [43] J.O.A. Robertsson, J.O. Blanch, W.W. Symes, C.S. Burrus, Galerkin-wavelet modeling of wave propagation: optimal finite difference stencil design, *Math. Comput. Model.* 19 (1994) 31–38.
- [44] J.H. Zhang, Z.X. Yao, Optimized finite-difference operator for broadband seismic wave modeling, *Geophysics* 78 (2013) A13–A18.
- [45] J.H. Zhang, Z.X. Yao, Optimized explicit finite-difference schemes for spatial derivatives using maximum norm, *J. Comput. Phys.* 250 (2013) 511–526.
- [46] S.L. Liu, X.F. Li, W.S. Wang, M.W. Lu, M.G. Zhang, Optimal symplectic scheme and generalized discrete convolutional differentiator for seismic wave modeling, *Chin. J. Geophys.* 56 (2013) 2452–2462 (in Chinese).
- [47] S.L. Liu, X.F. Li, W.S. Wang, Y.S. Liu, M.G. Zhang, H. Zhang, A new kind of optimal second-order symplectic scheme for seismic wave simulations, *Sci. China Earth Sci.* 57 (2014) 751–758.
- [48] W. Heinrichs, Improved Lebesgue constants on the triangle, *J. Comput. Phys.* 207 (2005) 625–638.
- [49] J. Proriot, Sur une famille de polynômes à deux variables orthogonaux dans un triangle, *C. R. Acad. Sci., Paris* 245 (1957) 2459–2461 (in French).
- [50] T. Koornwinder, Two-variable analogues of the classical orthogonal polynomials, in: R. Askey (Ed.), *Theory and Applications of Special Functions*, Academic Press, San Diego, 1975.
- [51] M. Dubiner, Spectral methods on triangles and other domains, *J. Sci. Comput.* 6 (1991) 345–390.
- [52] M.P. Appell, Sur une classe de polynômes, *Ann. Sci. Éc. Norm. Supér.* 9 (1980) 119–144 (in French).
- [53] M. Anshelevich, Appell polynomials and their relatives, *Int. Math. Res. Not.* 65 (2004) 3469–3531.
- [54] J.D. de Basabe, M.K. Sen, Grid dispersion and stability criteria of some common finite-element methods for acoustic and elastic wave equations, *Geophysics* 72 (2007) T81–T95.
- [55] I. Mazzieri, F. Rapetti, Dispersion analysis of triangle-based spectral element methods for elastic wave propagation, *Numer. Algorithms* 60 (2012) 631–650.
- [56] T. Liu, M.K. Sen, T. Hu, J.D. de Basabe, L. Li, Dispersion analysis of the spectral element method using a triangular mesh, *Wave Motion* 49 (2012) 474–483.
- [57] T. Melvin, A. Staniforth, J. Thuburn, Dispersion analysis of the spectral element method, *Q. J. R. Meteorol. Soc.* 138 (2012) 1934–1947.
- [58] S.L. Liu, X.F. Li, Y.S. Liu, T. Zhu, M.G. Zhang, Dispersion analysis of triangle-based finite element method for acoustic and elastic wave simulations, *Chin. J. Geophys.* 57 (2014) 2620–2630 (in Chinese).
- [59] D.P. Cao, J.K. Zhou, X.Y. Yin, The study for numerical dispersion and stability of wave equation with triangle-based finite element algorithm, *Chin. J. Geophys.* 58 (2015) 1717–1730 (in Chinese).
- [60] S.C. Brenner, L.R. Scott, *The Mathematical Theory of Finite Element Methods*, Texts Appl. Math., Springer, 2002.
- [61] D.S. Watkins, *Fundamentals of Matrix Computations*, 2nd ed., Pure Appl. Math., John Wiley and Sons, 2002.
- [62] M. Briani, A. Sommariva, M. Vianello, Computing Fekete and Lebesgue points: simplex, square, disk, *J. Comput. Appl. Math.* 236 (2012) 2477–2486.
- [63] R.M. Alford, K.R. Kelly, D.M. Boore, Accuracy of finite difference modeling of the acoustic wave equation, *Geophysics* 39 (1974) 834–842.
- [64] P. Moczo, J. Kristek, L. Halada, 3D fourth-order staggered-grid finite-difference schemes: stability and grid dispersion, *Bull. Seismol. Soc. Am.* 90 (2000) 587–603.
- [65] N. Tordjman, Éléments finis d'ordre élevé avec condensation de masse pour l'équation des ondes, Ph.D. thesis (in French), L'Université Paris IX Dauphine, 1995.
- [66] P. Keast, J.C. Diaz, Fully symmetric integration formulas for the surface of the sphere in s dimensions, *SIAM J. Numer. Anal.* 20 (1983) 406–419.
- [67] P. Keast, Moderate-degree tetrahedral quadrature formulas, *Comput. Methods Appl. Mech. Eng.* 55 (1986) 339–348.
- [68] P. Keast, Cubature formulas for the surface of the sphere, *J. Comput. Appl. Math.* 17 (1987) 151–172.
- [69] G. Cohen, *Higher Order Numerical Method for Transient Wave Equations*, Springer-Verlag, Berlin, 2002.
- [70] Y.H. Dai, Y. Yuan, A nonlinear conjugate gradient method with a strong global convergence property, *SIAM J. Optim.* 10 (1999) 177–182.
- [71] J. Nocedal, S.J. Wright, *Numerical Optimization*, Springer-Verlag, 1999.
- [72] W.W. Hager, H.C. Zhang, A new conjugate gradient method with guaranteed descent and an efficient line search, *SIAM J. Optim.* 16 (2005) 170–192.
- [73] W.W. Hager, H.C. Zhang, A survey of nonlinear conjugate gradient methods, *Pac. J. Optim.* 2 (2006) 335–358.
- [74] M.J. Khun, A numerical study of Lamb's problem, *Geophys. Prospect.* 33 (1985) 1103–1137.
- [75] J. Bérenger, A perfectly matched layer for the absorption of electromagnetic waves, *J. Comput. Phys.* 114 (1994) 185–200.
- [76] J. Chen, R.P. Bording, E. Liu, Z. Zhang, J. Badal, The application of the nearly optimal sponge boundary conditions for seismic wave propagation in poroelastic media, *J. Seism. Explor.* 19 (2010) 1–19.
- [77] E. Zhebel, S. Minisini, A. Kononov, W.A. Mulder, A comparison of continuous mass-lumped finite elements with finite differences for 3-D wave propagation, *Geophys. Prospect.* 62 (2014) 1111–1125.
- [78] A.T. de Hoop, A modification of Cagniard's method for solving seismic pulse problems, *Appl. Sci. Res. B* 8 (1960) 349–356.